JGR Earth Surface

RESEARCH ARTICLE
10.1029/2021JF006163

Topographic and Geologic Controls on Frost Cracking in Alpine Rockwalls

Daniel Draebing[1,2,3] **and Till Mayer**[1,3]

[1]Chair of Geomorphology, University of Bayreuth, Bayreuth, Germany, [2]Department of Physical Geography, Utrecht University, Utrecht, Netherlands, [3]Chair of Landslide Research, Technical University of Munich, Munich, Germany

Key Points:

- Temperature loggers provide rock temperature data that incorporates topographic effects on insolation and insulation
- Sensitivity tests on frost cracking models showed differences of frost magnitude while frost cracking depth patterns were consistent
- Thermo-mechanical models incorporating rock strength and hydraulic properties produced more realistic altitudinal frost cracking patterns

Supporting Information:

Supporting Information may be found in the online version of this article.

Correspondence to:

D. Draebing,
d.draebing@uni-bayreuth.de

Citation:

Draebing, D., & Mayer, T. (2021). Topographic and geologic controls on frost cracking in Alpine rockwalls. *Journal of Geophysical Research: Earth Surface*, *126*, e2021JF006163. https://doi.org/10.1029/2021JF006163

Received 12 MAR 2021
Accepted 18 MAY 2021

Abstract Frost weathering is a major control on rockwall erosion in Alpine environments. Previous frost cracking model approaches used air temperatures as a proxy for rock temperatures to drive frost weathering simulations on rockwall and on mountain scale. Unfortunately, the thermal rockwall regime differs from air temperature due to topographic effects on insolation and insulation, which affects frost weathering model results and the predicted erosion patterns. To provide a more realistic model of the rockwall regime, we installed six temperature loggers along an altitudinal gradient in the Swiss Alps, including two logger pairs at rockwalls with opposing aspects. We used the recorded rock surface temperatures to model rock temperatures in the upper 10 m of the rockwalls and as input data to run four different frost cracking models. We mapped fracture spacing and rock strength to validate the model results. Our results showed that frost cracking models are sensitive to thermal, hydraulic and mechanical parameters that affect frost cracking magnitude but frost cracking patterns in terms of peak location and affected rock mass remained consistent between varying input parameters. Thermo-mechanical models incorporate rock strength and hydraulic properties and provided a frost cracking pattern at the rockwall scale that better reflects the measured fracture spacing. At the mountain scale, these models showed a pattern of increasing frost cracking with altitude, which is contrary to purely thermal models but consistent with observations of existing rockfall studies.

Plain Language Summary Frost weathering is an important mechanism in shaping rockwalls in Alpine environments. Previous studies developed either purely thermal or thermo-mechanical models incorporating mechanical and hydraulic parameters to simulate this process. Both model types provide valuable insights about a process that is hard to measure. Previous model approaches used air temperature as input data. However, rock temperatures differ from air temperatures due to topography that changes the insolated surface of rockwalls and insulating snow cover. We measured rock temperatures directly at six rockwalls with different aspects along a large range of altitude. We used our data to run four existing frost weathering models. Our results show that rock type, the strength of rocks and water availability influence the frost weathering magnitude, but the location of cracking and the rockwall depth affected does not change. The frost cracking pattern should be reflected by the fracture network and the strength of rockwalls. We mapped fractures and measured rock strength and our results correspond better to thermo-mechanical model results. Thermo-mechanical model results show an increase in frost weathering with increasing altitude. This pattern is consistent with rockfall observations. In contrast, purely thermal models showed an inverse relationship with higher frost cracking at lower altitudes.

1. Introduction

The interplay of tectonic, climatic, and erosional processes controls topography and in turn steep alpine environments are characterized by high erosion rates (Montgomery & Brandon, 2002; Whipple et al., 1999). Climate affects mechanical weathering, including frost cracking processes (Eppes & Keanini, 2017), that breakdown rock (Matsuoka & Murton, 2008). This rock is subsequently transported by rockfall processes (Krautblatter & Dikau, 2007) and results in erosion of rockwalls. Rockwall erosion rates also depend on in situ stress, geological, hydrological, and biological conditions (Krautblatter & Moore, 2014). Field measurements of rockwall erosion using rockfall collectors suggest that rockfall is influenced by seasonal ice segregation (Matsuoka & Sakai, 1999; Sass, 2005c) and volumetric expansion caused by short-term freezing (Fahey & Lefebure, 1988; Matsuoka, 2019; Sass, 2005c), which both are controlled by moisture supply (Rode

et al., 2016; Sass, 2005a, 2005c). If rockfall deposits are not reworked by glaciers (e.g., Scherler et al., 2011) or rivers (e.g., Schrott et al., 2003), long-term rockfall results in scree slope formation (Statham, 1976). The spatial distribution of scree slopes suggests a climatic control on frost weathering on a regional scale (Hales & Roering, 2005; Thapa et al., 2017). Erosion rates derived from talus slopes (Sass, 2010) and spatially distributed rockfall collectors (Sass, 2005b) indicate an increase of rockfall supply from north-facing permafrost affected rockwalls on short-term (up to 5 years) and mid-term timescale (~400 years; Sass, 2010). On Holocene timescale, talus slope deposits suggest an increased rockwall erosion rate on north-facing compared to south-facing rockwalls (Sass, 2007). Terrestrial laser scanning and seismic monitoring data showed an increase in rockfall activity during freezing periods, suggesting that frost weathering acts as a preparatory and triggering factor of rockfall (e.g., Dietze et al., 2017; Strunden et al., 2015). In summary, frost weathering is a key agent of rockwall erosion. Rockfall presents hazards to humans and infrastructure (e.g., Evans & Hungr, 1993). Rockfall also provides material for debris flows that can propagate hazards down the sediment cascade to the valley bottom (Hirschberg et al., 2021; Rengers et al., 2020). Due to the link to climate, climate change will affect frost weathering activity and therefore alter rockwall erosion and the hazard potential of rockfall and debris flows.

The efficacy of different frost weathering processes has been discussed since the 1980s (McGreevy & Whalley, 1985; Walder & Hallet, 1986). Fractures in rock can grow when stresses exceed the strength properties of rock (critical cracking), but cracks can also grow steadily at stresses below critical levels (subcritical cracking) (Eppes & Keanini, 2017). Volumetric expansion by freezing ice occurs during short-term freezing cycles and can produce stresses as high as 207 MPa (Matsuoka & Murton, 2008), which would exceed the tensile strength of common rocks by one order of magnitude (Perras & Diederichs, 2014). Field measurements suggest that these processes occur during freezing periods in late autumn and due to refreezing of meltwater in late spring and summer (Matsuoka, 2001, 2008). Recently, Draebing and Krautblatter (2019) quantified the volumetric expansion of geometrically defined saturated fractures and demonstrated that the resulting stresses exceeded the strength properties of rocks. Therefore, volumetric expansion is highly effective but unlikely due to a lack of saturation of fractures in the field. In contrast, ice segregation occurs during sustained freezing conditions due to cryosuction-induced stresses (Matsuoka & Murton, 2008). Laboratory (Duca et al., 2014; Hallet et al., 1991; Murton et al., 2006) and field studies (Draebing, Krautblatter, & Hoffmann, 2017; Weber et al., 2018) support the importance of ice segregation for frost weathering. Draebing and Krautblatter (2019) tested the efficacy of ice segregation on fractured rock and ice segregation produced subcritical stresses below the strength threshold of rocks. The ice-induced stresses started to occur at a temperature between −0.04°C and −2.35°C depending on lithology (Draebing & Krautblatter, 2019) at pore water availability ranges that are common in Alpine rockwalls (Girard et al., 2013; Sass, 2005a). Field measurements of frost cracking and ice-induced crack widening at or near the rock surface (Amitrano et al., 2012; Draebing, Krautblatter, & Hoffmann, 2017; Girard et al., 2013) and in rock depths up to 20 m (Wegmann & Gudmundsson, 1999; Wegmann & Keusen, 1998) demonstrated that frost cracking occurs across the full temperature range between 0°C and −15°C. Sustained freezing results in higher frost cracking activity than frequent freeze-thaw cycling (Amitrano et al., 2012; Girard et al., 2013).

Different frost cracking models have been developed to model ice segregation induced weathering. Thermo-mechanical models include lithological and hydrological effects (Walder & Hallet, 1985) and were successfully used to model frost cracking at the laboratory (Murton et al., 2006) and rockwall scales (Sanders et al., 2012). At the landscape scale, it is difficult to relate the physics of ice growth to rock breakdown by frost cracking and rockwall erosion by rockfall, thus, controlling rock hydraulic, thermal and mechanical parameters are difficult to obtain. A simple empirical frost cracking model using elevation dependent air temperature was developed by Hales and Roering (2007) to model spatial and temporal patterns of rockwall erosion. This model was applied in studies in the European Alps (Delunel et al., 2010; Messenzehl et al., 2018; Savi et al., 2015), New Zealand Alps (Hales & Roering, 2009), Himalayas (Orr et al., 2019; Scherler, 2014), and the Oregon Coast range (Marshall et al., 2015, 2017). Resulting frost cracking intensity (FCI) was validated using fracture spacing as a proxy for rock mass susceptibility to frost weathering (Hales & Roering, 2007, 2009; Messenzehl et al., 2018) or compared to erosion rates (Delunel et al., 2010; Marshall et al., 2015, 2017; Savi et al., 2015). Anderson et al. (2013) extended the model to simulate long-term development of periglacial landscapes. Recently, Rempel et al. (2016) developed a thermo-mechanical model based on the model by Walder and Hallet (1985) to incorporate ice physics without losing applicability at

geomorphic scales. Marshall et al. (2021) applied the model in combination with climate simulations to model frost weathering in unglaciated North America during the Last Glacial Maximum. The different models use air temperature as a proxy for rock temperature (e.g., Hales & Roering, 2007; Rempel et al., 2016), but previous permafrost studies demonstrated that there is a significant temperature offset between air and rockwall temperature (e.g., Hasler, Gruber, & Haeberli, 2011; Magnin et al., 2015).

All frost cracking models assume thermal, hydrologic and mechanical properties of rocks. We define these rock properties as geological control in this paper. Previous studies have not yet tested how these properties influence model results at the rockwall and mountain scales. For this purpose, we installed six rock temperature loggers along an altitudinal transect including different aspects and different lithology. We used the obtained rock temperature data to (a) model frost cracking activity at the rockwall scale by applying the models by Hales and Roering (2007), Anderson et al. (2013), Walder and Hallet (1985) and Rempel et al. (2016). We (b) tested the sensitivity of these model results to rock thermal diffusivity, hydraulic properties, initial crack length and fracture toughness to identify if observed frost cracking patterns are an artifact of a limited range of input parameters. We (c) mapped fracture spacing and quantified rock strength in the field as a proxy for frost weathering, compared the data to frost cracking model results on rockwall and mountain scale. We ultimately discussed the implications of climate change on frost weathering.

2. Study Site

Our research was conducted in the Hungerli Valley and Steintaelli, Swiss Alps (Figure 1). The Hungerli Valley is an east-to-west oriented hanging valley of the Turtmann Valley (Figure 1c), while the Steintaelli is a 50 m northeast (NE) to southwest (SW) orientated ridge on the crestline between Matter and Turtmann Valley (Figure 1b). The lithology consists of paragneiss, mainly schisty quartz slate with inclusions of aplite and quartzite in the Rothorn (RH) cirque and amphibolite in the Hungerlihorli (HH, Figure 1c; Bearth, 1980). Rockwalls reach from 2,400 m up to the Rothorn at 3,277 m. Adjacent to the rockwalls, talus slopes formed by rockfall processes store one fifth of the sediment of the Hungerli Valley (Otto et al., 2009). In the Steintaelli, geophysical measurements indicated the occurrence of permafrost on the NE-facing slope, while permafrost was absent in the SW slope between 2006 and 2019 (Draebing, Haberkorn, et al., 2017; Krautblatter & Draebing, 2014; Scandroglio et al., 2021). Permafrost distribution is strongly controlled by snow cover, which resulted in 3.7°C–3.9°C colder mean annual rock surface temperature (MARST) at the NE compared to SW slope (Draebing, Haberkorn, et al., 2017). Snow cover influenced cryogenic and thermal processes that resulted in fracture opening due to ice segregation on the crest and thermal induced fracture dynamics on the SW slope (Draebing, Krautblatter, & Hoffmann, 2017).

3. Methods

We conducted measurements on rockwalls ranging from 2,580 to 3,158 m to identify the influence of altitude on frost weathering (Figure 2a). To determine the influence of aspect, we investigated two rockwalls (RW1 and RW3) at similar altitudes with opposing north and south expositions.

3.1. Rockwall and Rock Mechanical Data

We collected several 0.4 × 0.2 × 0.15 m large schisty quartz slate samples from the talus slope below RW4, amphibolite samples below RW3-N and aplite samples below RW2. We assumed that talus slope samples represented the mechanical properties of the adjacent rockwalls. To calibrate mechanical frost cracking model parameters in the laboratory, we quantified rock sample anisotropy (Draebing & Krautblatter, 2012), Poisson's ratio ν, and shear modulus G using seismic laboratory measurements (see Text S1 and Table S2 in the supporting information). We derived uniaxial compressive strength σ_u (Mutschler, 2004), tensile strength σ_t (Lepique, 2008), and estimated fracture toughness K_C (Chang et al., 2002; Zhang, 2002). To calibrate the heat transfer model, rock porosity φ_r and density ρ_r were measured following the German industry norm (DIN 52102 and DIN EN 1097-6).

In the field, we conducted horizontal and vertical scanline measurements (Priest, 1993) at RW2 to RW4 and reanalyzed previously conducted measurements at RW1 (Halla, 2013). Based on these measurements,

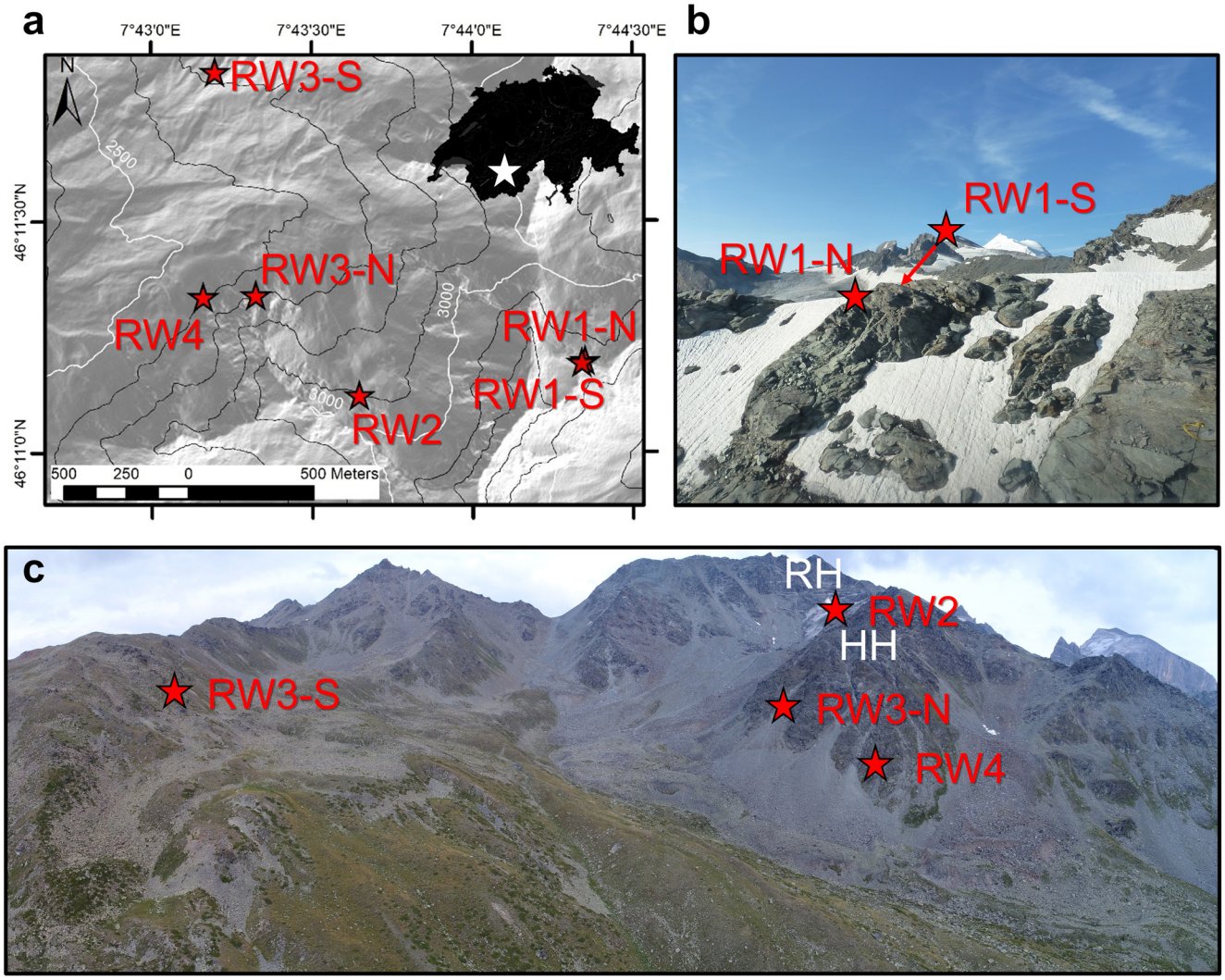

Figure 1. (a) The research area is located in the Swiss Alps (inset map). Hillshade map shows the locations of instrumented rockwalls (Swiss Alti3D 2 m DEM provided by the Federal Office of Topography, swisstopo). Overview photos of the (b) the Steintaelli ridge and (c) Hungerli Valley. Red stars highlight the location of temperature loggers; RH and HH indicate the Rothorn and Hungherlihorli peaks.

we calculated the fracture spacing (Priest, 1993), which will be compared to the lower limit, depth range and peak location of modeled frost cracking (Figure 2c) to validate the effect of frost cracking (Hales & Roering, 2007, 2009; Messenzehl et al., 2018). We quantified rock strength using Schmidt hammer measurements (Selby, 1980), which are a common tool to quantify effects of near surface weathering (McCarroll, 1991; Murphy et al., 2016; Shobe et al., 2017) including frost weathering (Matsuoka, 2008; Matthews et al., 1986). We compared measured rock strength to near surface model results of frost cracking.

3.2. Meteorological and Rock Temperature Data

We used air temperature (AT) and snow depth data obtained from the meteo station Oberer Stelligletscher (2,910 m), located on flat terrain 2–3 km southeast (SE) of our study area in the Matter Valley (MeteoSwiss, 2019b). The data shows a gap from mid-January to end of February 2018 (Figure 3a), probably as a result of intense snow depth (>3.5 m). To fill the gap, we adapted AT from near-by (6.5 km) meteo station Grächen (MeteoSwiss, 2019a), located at 1,605 m in the Matter Valley using a linear correlation ($r^2 = 0.85$). The temperature adjustment corresponds to a lapse rate of 6°C km^{-1}.

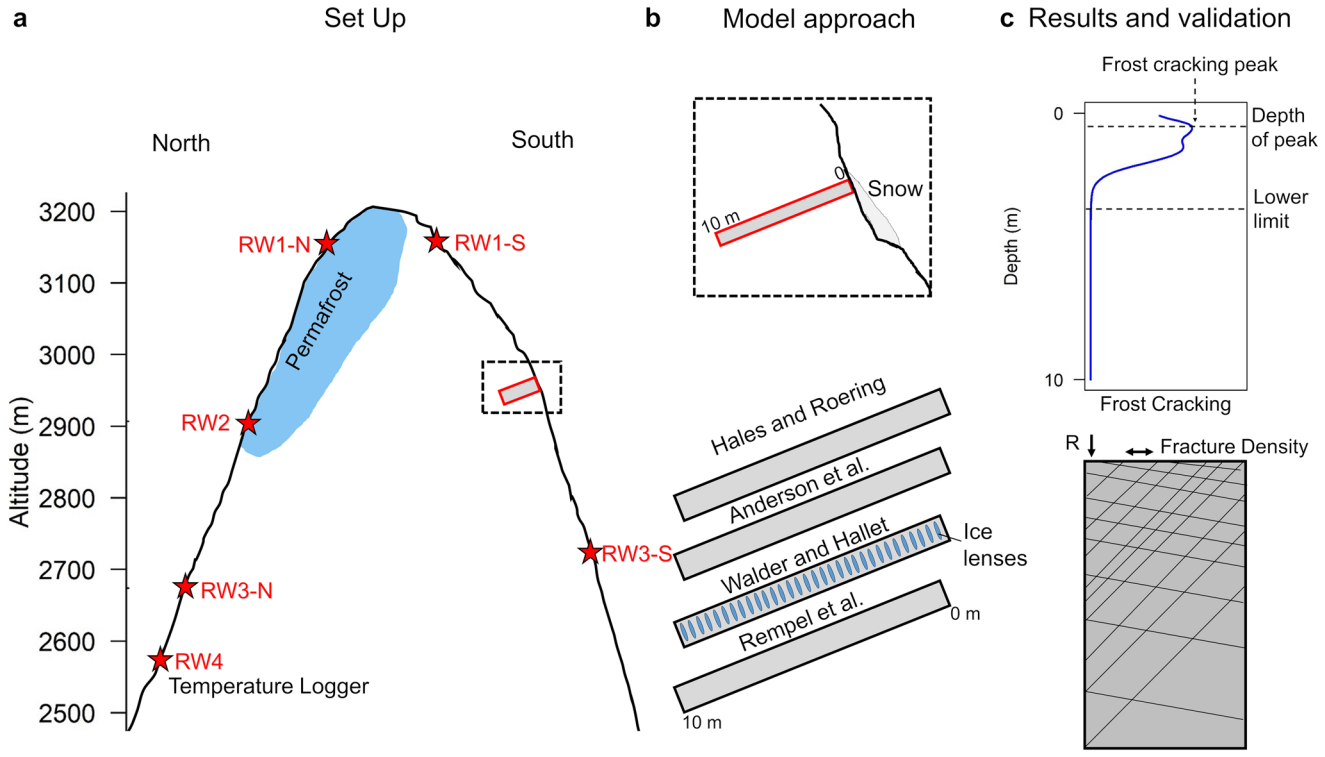

Figure 2. We investigated frost weathering along a topographical gradient. (a) Schematic illustration of our research set up with installed rock temperature loggers (red stars) on rockwalls ranging from ~2,500 to 3,200 m covering North and South rockwall aspects. (b) In our model approach, we used rock surface temperature data from our loggers to run 1D rock thermal models and used four different frost cracking models to simulate frost weathering. (c) Frost weathering model results are interpreted in terms of the depth location of the frost cracking peak and the lower limit of frost cracking. Modeling results are compared to fracture density mapping and Schmidt hammer measurements (R).

Rock surface temperatures (RSTs) depend on topography, snow cover, fracturing and water availability. Topography changes the insolated geometry and results in solar radiation differences (Gruber et al., 2004; Hasler, Gruber, & Haeberli, 2011), while snow cover can build up from ledges and reach a thickness of several meters at rockwalls (Haberkorn et al., 2017; Phillips et al., 2017; Wirz et al., 2011) insulating the rock surface (Haberkorn, Hoelzle, et al., 2015; Haberkorn, Phillips, et al., 2015). Fracturing increases surface roughness and the ability to retain snow (Gruber & Haeberli, 2007), increases convective heat flow by air (Moore et al., 2011) and advective heat flow by water (Gruber & Haeberli, 2007; Hasler, Gruber, Font, & Dubois, 2011; Phillips et al., 2016) as well as water availability and permeability (Dietrich et al., 2005; Gruber & Haeberli, 2007). To monitor RST, we installed six Maxim iButton DS1922 L temperature loggers in 10 cm deep boreholes following methods developed by previous studies (e.g., Draebing, Haberkorn, et al., 2017; Haberkorn, Phillips, et al., 2015). These temperature loggers have a nominal accuracy of ±0.5°C according to the manufacturer, but zero curtain occurrence suggest an accuracy of ±0.25°C at the freezing point. The loggers recorded RST in 3 h intervals between September 1, 2016 and August 31, 2019 (RW2, RW3-N, and RW4) or between September 1, 2017 and August 31, 2019 (RW1-N, RW1-S, and RW3-S), respectively. Snow cover and zero curtain duration can be detected in RST time series using daily standard deviations due to insulating properties of snow (Haberkorn, Hoelzle, et al., 2015; Schmid et al., 2012). We applied the uniform standard deviation threshold of <0.5 K for positive and negative RST by Haberkorn, Phillips, et al. (2015), which was previously validated in a study in the Steintaelli (Draebing, Haberkorn, et al., 2017). We calculated the mean annual air temperature (MAAT) and adapted AT to logger elevations by using the temperature lapse rate. To compare temperature logger locations, we calculated the MARST. We calculated mean winter and mean summer air/rock surface temperatures to analyze seasonal effects. We calculated a 10-days running average of air and RSTs and calculated the thermal offset that should reflect insolation and insulation effects.

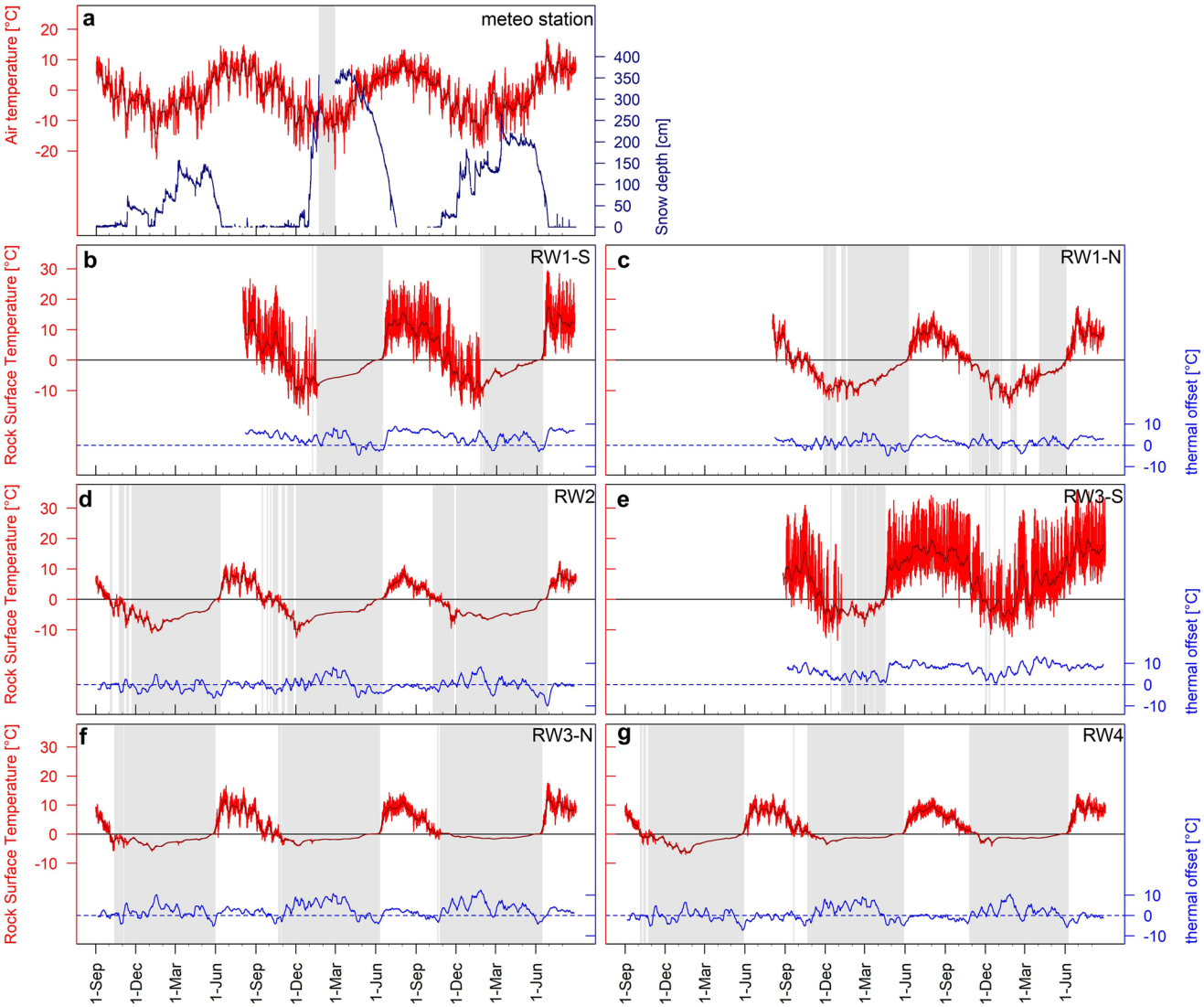

Figure 3. (a) Air temperature and snow depth data from the meteorological station Oberer Stelligletscher located at 2,910 m for the period ranging from September 1, 2016 to August 31, 2019. The light gray rectangle highlights the interpolated air temperature used to fill a data gap. (b–g) Rock surface temperature (red lines), running 10-days mean rock surface temperature (dark red lines) and running 10-days thermal offset (blue lines) for the measurement period between 2016 and 2019. Rockwalls are arranged along the topographical gradient from 3,158 to 2,580 m. Light gray rectangles highlight the snow cover period.

To model rock temperatures up to 10 m depth in 0.1 m resolution intervals, we used a 1D conductive heat model applying the Fourier Equation (Carslaw & Jaeger, 1986) and incorporated latent heat effects, per previous studies (e.g., Anderson et al., 2013; Hipp et al., 2014). Measured rock porosity of the rock samples were below 1% (Table 2). In contrast to intact rock samples, rock masses of rockwalls consist of fractures. These fractures are incorporated into the model by increasing the rockwall porosity to 3% as done in previous rock temperature model approaches (e.g., Draebing, Haberkorn, et al., 2017; Noetzli & Gruber, 2009; Noetzli et al., 2007; Wegmann & Keusen, 1998; Wegmann et al., 1998). We assume isotropic rock properties and that pores and fractures are fully saturated (e.g., Rempel et al., 2016; Walder & Hallet, 1985). For details on the model-processing see Text S2 in the supporting information and for used parameters see Table 2.

3.3. Frost Cracking Modeling

To evaluate frost weathering in the six rockwalls studied, we used our rock temperature data to drive four different frost weathering model approaches. The purely thermal models developed by Hales and

Roering (2007; HR-Model) and Anderson et al. (2013; A-Model)) assume that the frost cracking rate by ice segregation is proportional to the temperature gradient and therefore they use the temperature gradient as a proxy for cracking intensity. Both model approaches assume that frost cracking will occur in a temperature range between −8°C and−3°C termed the frost cracking window (FCW) by Anderson (1998). The second assumption is water availability. In the Hales and Roering (2007) model, water is available when RSTs are above 0°C (upper boundary) and the temperature gradient is negative. Additionally, water availability from groundwater is defined as rock temperatures at 10 m depth are above 0°C (lower boundary) and when the temperature gradient is positive. The model by Anderson et al. (2013) assumes water is available at a rock temperature above 0°C anywhere along the one-dimensional path inside the rock mass, but water transport is restricted by a penalty function that modifies the modeled temperature gradients depending on their distance to the next water reservoir. If the temperature and water assumptions are fulfilled, both models sum up the temperature gradients and use this as a proxy for frost cracking.

We used two thermo-mechanical models to simulate frost weathering at rockwalls. Both models assume that a rockwall consists of pores of different shapes and sizes including non-equant voids called cracks. In their model, Walder and Hallet (1985; WH-Model) assumed cracks have a penny-shaped form with an initial crack radius x_i of 0.05 m, which corresponds to a crack length of 0.1 m, and a crack plane parallel to the rockwall ($\varphi_p = 0°$). These cracks are spaced widely enough to enhance independent growth. All cracks grow in a mode I form along the plane of the crack purely by ice pressure. In our model approach, we assumed the existence of an independent crack at every model increment step of 0.1 m rock depth (Figure 2b). The model further assumes that the pore space of unfrozen rock is fully saturated at all times. Segregation ice growth starts for temperatures below the freezing point in pores $T_f = -1$°C, but only if an unfrozen rock mass area with water is available ($T > T_f$). One-dimensional water migration in the model is restrained by the thermal gradient and the grain/pore surface resistivity (Text S3 in the supporting information). When ice pressure rises in the ice lens, an elastic opening of the crack occurs and deforms the crack into an oblate ellipsoid. Crack length grows inelastically if one third of the critical fracture toughness (K_c) is reached. We used hydraulic and mechanical parameters suggested by Walder and Hallet (1985) except for Poisson's ratio, shear modulus and critical fracture toughness, which we measured in the laboratory (Table 2). To enable an annual comparison of crack growth, we started the simulation with an initial crack length of 0.1 m for every year (September 1 to August 31) to ensure comparability between years. We summed up the final crack length at each year and divided this length by the rock depth of our model to get a quantitative measure to compare frost cracking at different rockwalls.

The model by Rempel et al. (2016) assumes a porosity change to occur alongside frost weathering. The authors determine an upper temperature limit ΔT_c for ice segregation depending on fracture toughness and crack radius (see Text S4 in the supporting information) and a lower limit of ice segregation controlled by permeability dependent water availability. We use the values suggested by Rempel et al. (2016; R-Model; Table 2), unfrozen permeability measured by Krautblatter (2009) and laboratory defined critical fracture toughness. Rempel et al. (2016) integrate porosity change over depth to get the total expansion Λ resulting from ice segregation.

3.4. Sensitivity of Frost Cracking Models

All frost cracking models are sensitive to the temperature gradient. The temperature gradient results from the rock temperature modeling using the Fourier equation that propagated heat using rock thermal diffusivity $\kappa\,(= k/c\rho_r)$, which depends on rock thermal conductivity k, rock specific heat capacity c and rock density ρ_r. All parameters show a variation on rock sample scale, which will increase on rockwall scale. Therefore, rock thermal diffusivity comprises a range of values and we used a mean value for frost cracking modeling. To test the sensitivity to heat conduction, we additionally modeled the frost cracking using minimum and maximum values of rock diffusivity (Table 2).

The thermo-mechanical models by Walder and Hallet (1985) and Rempel et al. (2016) are in addition sensitive to hydraulic parameters such as conductivity or permeability, initial crack length and fracture toughness. Hydraulic permeability values range over magnitudes such as 10^{-18} to 10^{-12} m^2 (Rempel et al., 2016). We use the nominal value 10^{-14} m^2 by Rempel et al. (2016) and the measured value 10^{-18} m^2 by Krautblatter (2009)

Table 1
Altitude, Exposition, Slope Angle, Lithology, 1st to 3rd Quartile and Mean of Rock Strength Measured With the Schmidt Hammer, and 1st to 3rd Quartile and Mean of Fracture Spacing of Instrumented Rockwalls

					Rock strength (R)	Fracture spacing (m)
Rockwall	Altitude (m)	Exposition (°)	Slope (°)	Lithology	1st–3rd Qu. (Mean)	1st–3rd Qu. (Mean)
RW1-S	3,158	154	79	Quartz Slate	45–58 (53)	1.65–2.98 (2.82)
RW1-N	3,157	33	90	Quartz Slate	45–48 (46)	0.24–1.16 (0.85)
RW2	2,907	70	78	Aplite	46–52 (49)	0.12–0.50 (0.37)
RW3-S	2,723	148	71	Quartz Slate	30–34 (31)	0.10–0.41 (0.32)
RW3-N	2,674	311	85	Amphibolite	59–68 (64)	0.13–0.52 (0.43)
RW4	2,580	17	87	Quartz Slate	37–42 (39)	0.31–1.00 (0.67)

for the sensitivity test of the R-Model. To test the sensitivity of the WH-Model to hydraulic properties, we increased the applied hydraulic conductivity (5×10^{-14} m s^{-1}) by four orders of magnitude to include a similar variation as in the R-Model. Crack length varies in rocks (Maji & Murton, 2020) and needs to be assumed, therefore, we conducted tests using a crack length of 0.01 and 0.1 m. Fracture toughness varies between rock types and comprises a wide range within each rock type (Atkinson, 1984). For our model approach, we used a mean value of fracture toughness derived from an estimation based on uniaxial strength measurements (Chang et al., 2002). For the sensitivity tests, we used in addition a minimum and maximum value (Table 2). The minimum value was derived from the Schmidt hammer tests (Table S1) according to ISRM (1978). We estimated the maximum value based on tensile strength measurement on rock samples (Zhang, 2002).

4. Results

4.1. Rockwall Mechanical Properties

We used the Schmidt hammer rebound value R as a proxy for rock strength. Observed mean rock strength was highest at RW3-N (64, Table 1, Figure 5ad), which consists of amphibolite. Rockwalls consisting of schisty quartz slate showed a variation of mean rock strength and ranged from 31 at RW3-S (Figure 5x), 39 at RW4 (Figure 5aj), 46 at RW1-N (Figure 5l) to 53 at RW1-S (Figure 5f). RW2 that comprise aplite had a mean rock strength of 49 (Figure 5r). Mean fracture spacing showed large spatial variation within schisty quartz slate rock masses ranging from 0.32 m at RW3-S, 0.67 m at RW4, 0.85 m at RW1-N to 2.82 m at RW1-S (Table 1, Figures 7a–7d). Aplite and amphibolite rock masses possessed a mean fracture spacing of 0.37 and 0.43 m, respectively.

4.2. Meteorological, Rock Surface and Rock Temperature Data

The meteorological station located at 2,910 m recorded a MAAT between −1.1°C and −0.6°C (Table 3). In winter, mean winter air temperature (MWAT) ranged from −6.5°C to −9.1°C, while mean summer air temperature (MSAT) was 5.9°C–6.8°C in summer. Snow cover ranged between 216 and 246 days (Table 3), onset was around mid-November and snow cover lasted until mid-June. Recorded snow depth on flat terrain reached between 157 and 371 cm (Figure 3a). RSTs followed the annual and daily oscillation of ATs (Figures 3b–3g). The MARST showed no clear altitudinal trend with decreasing temperatures at higher locations as expected from AT trends (Table 3). South-facing rockwalls revealed warmer MARST than north-facing rockwalls and ranged between 2.2°C and 2.5°C at RW1 at 3,157 m and between 4.6°C and 6°C at RW3 at ∼2,700 m. The altitudinal difference between north and south-facing loggers at RW3 is 50 m, which corresponds to 0.3°C colder conditions at the higher located south-facing rockwall. At north-facing rockwalls, mean winter rock surface temperature (MWRST) showed an increase with decreasing altitude. South-facing rockwalls showed 0.5°C–1.6°C warmer winter conditions than north-facing rockwalls, however the logger located at RW3-S recorded −1.8°C colder temperatures in 2017/18 than RW3-N. Mean summer rock surface temperature (MSRST) showed no elevation pattern and highest values were recorded at RW1-N.

Table 2
Model Parameters

Parameter		Aplite	Amphibolite	Quartz slate
		Value (range)	Value (range)	Value (range)
All models				
Rock density (kg m^{-3})	ρ_s	2,760	2,970	2,800
Assumed (measured) rock porosity (%)	n_r	3 (0.89 ± 0.02)	3 (0.52 ± 0.11)	3 (0.80 ± 0.17)
Rock thermal conductivity[a] (W m^{-1} K^{-1})	λ_s	2.8 (1–3.8)	1.54 (1.3–1.7)	2.5 (1–4.1)
Rock specific heat capacity[a] (kJ kg^{-1} K^{-1})	c_s	0.80 (0.67–1.05)	0.75 (0.67–0.88)	0.80 (0.67–1.05)
Rock thermal diffusivity (m^2 s^{-1})	κ	1.23 (0.33–1.99)	0.67 (0.49–0.83)	1.08 (0.33–2.12)
Latent heat (kJ kg^{-1})	L		334	
Rock water content (%)	W		3	
Water content below pore freezing point[b] (%)	W_u		5	
Ice density (kg m^{-3})	ρ_i		920	
Ice thermal conductivity (W m^{-1} K^{-1})	λ_i		2.24	
Ice specific heat capacity (kJ kg^{-1} K^{-1})	c_i		2.09	
Water density (kg m^{-3})	ρ_w		1,000	
Water thermal conductivity (W m^{-1} K^{-1})	λ_w		0.56	
Water specific heat capacity (kJ kg^{-1} K^{-1})	c_w		4.18	
Thermo-mechanical models				
Critical fracture toughness[d]* (MPa $m^{1/2}$)	K_C	1.9 (1.6–2.1)	2.2 (1.9–3.1)	1.7 (1.3–2.0)
Walder and Hallet (1985)				
Pore freezing point[c] (°C)	T_f		−1	
Hydraulic conductivity[c] (m s^{-1})	k_{hc}		5×10^{-14}	
Grain size[c] (mm)	R		0.75	
Liquid layer thickness[c] (nm $°C^{1/2}$)	h_l		6	
Initial crack radius[c] (m)	x_i		0.05	
Angle between crack plane and rockwall[c] (°)	ϕ		0	
Poisson's ratio ()	ν	0.339	0.3205	0.263
Shear modulus (GPa)	G	16.73	35.34	23.05
Growth-law parameter[d] (m s^{-1})	V_c	340	340	340
Growth-law parameter[c] ()	γ	37.1	37.1	37.1
Rempel et al. (2016)				
Bulk melting temperature[e] (K)	T_m		273	
Unfrozen permeability[f] (m^2)	k_{p0}		10^{-18} (10^{-18}–10^{-14})	
Power law exponent[e] ()	α		4	
Undercooling for ice formation[e] (°C):	ΔT_f		0.1	

[a]Cermák and Rybach (1982). [b]Anderson et al. (2013). [c]Walder and Hallet (1985) with values from Atkinson and Rawlings (1981), Gilpin (1979, 1980) and Segall (1984). [d]Draebingand Krautblatter (2019). [e]Rempel et al. (2016) with values from Andersland and Ladanyi (2004). [f]Krautblatter (2009), *this study.

South-facing rockwalls revealed 1.9°C–2.1°C warmer conditions at RW1 that increased to 8.5°C–8.6°C difference at RW3.

The annual temperatures of north-exposed rockwalls revealed an amplitude increase with increasing altitude (Figures 3c, 3d, 3f, and 3g), which was between −7.0°C and 13.9°C at RW4 at 2,580 m and −15.6°C and 17.6°C at RW1-N at 3,157 m. The annual temperature amplitude was increased at south-facing rockwalls and was between −17.8°C and 29.4°C at RW1-S and −12°C and 32°C at RW3-S. At daily scale, loggers at

Table 3
Mean Annual Air Temperature (MAAT), Mean Annual Rock Surface Temperature (MARST), Snow Duration, Mean Winter Air Temperature (MWAT), Mean Winter Rock Surface Temperature (MWRST), Mean Summer Air Temperature (MSAT), and Mean Summer Rock Surface Temperature (MSRST) Values for Meteorological Station and Temperature Loggers

	MAAT/MARST (°C)			Snow duration (d)			MWAT/MWRST (°C)			MSAT/MSRST (°C)		
Logger	2016/17	2017/18	2018/19	2016/17	2017/18	2018/19	2016/17	2017/18	2018/19	2016/17	2017/18	2018/19
Meteo Station	−0.6	−1.0	−1.1	216	225	246	−6.5	−9.1	−7.1	6.6	5.9	6.8
RW1-S[a]	NA	0.3	1.4	NA	150	138	NA	−7.3	−6.9	NA	9.3	10.1
RW1-N[a]	NA	−1.9	−1.1	NA	161	120	NA	−8.8	−8.5	NA	7.4	8.0
RW2	−1.7	−1.7	−1.4	207	224	245	−7.5	−6.3	−5.3	5.9	4.2	4.3
RW3-S[b]	NA	5.6	7.8	NA	81	5	NA	−4.1	−0.7	NA	15.9	16.2
RW3-N	0.9	1.0	1.8	228	227	233	−3.6	−2.3	−1.2	8.6	7.3	7.7
RW4	0.7	1.5	1.8	220	220	223	−4.4	−1.8	−1.6	7.6	7.3	7.4

Abbreviations: MAAT, Mean annual air temperature; MARST, Mean annual rock surface temperature; MSAT, Mean summer air temperature; MSRST, Mean summer rock surface temperature; MWAT, Mean winter air temperature; MWRST, Mean winter rock surface temperature.
[a]August 29, 2017–August 28, 2019. [b]2017/18–2018/19.

north-facing rockwalls measured small daily temperature variations up to 4°C, whereas loggers at south-exposed rockwalls recorded variations up to 16.5°C. Snow cover attenuated daily temperature oscillations with expected high deviation between north- and south-exposed rockwalls. At north-facing rockwalls, snow cover started between October and December and lasted between 220 and 251 days (RW2) per year with only minor differences between RW2-RW4 and individual years (Figures 3d, 3f, and 3g). An exception was the highest rockwall RW1-N with only 120–160 days (Figure 3c). At south-facing rockwalls, snow onset was delayed to mid-November and February and snow cover duration was reduced to 138–164 days at RW1-S and between 5 and 85 days at RW3-S (Figures 3b and 3e).

The thermal offset is characterized as the temperature difference between measured 10-days average RST and modeled 10-days average AT adjusted to rockwall altitude. RST at south-facing rockwalls are usually warmer than AT during snow-free periods resulting in a positive thermal offset (Figures 3b and 3e). At north-facing rockwalls, the thermal offset fluctuated around zero during snow-free periods (Figures 3c, 3d, 3f, and 3g). Following snow onset, the thermal offset was positive indicating warmer RST than AT. The thermal offset reversed to negative temperatures at half or two third of the snow cover period and RST were colder than ATs.

Temperature regimes inside our rockwalls showed a typical attenuated and shifted development of rock temperature with the warmest and coldest temperatures at the surface (Figure 4). The results revealed that positive temperatures reached seasonally down to 2.5 m depths at RW2 and to 3.5 m at RW1-N, while the rock mass below showed continuous negative rock temperatures for the entire study period (Figures 4b and 4c). In contrast, south-facing and lower elevated north-facing rockwalls experienced seasonal freezing, while rock temperatures below 1.2 and 5.5 m depths, respectively, remained positive throughout the measurement period (Figures 4a, 4d–4f). Maximum summed annual temperature gradients at north-facing rockwalls reached from 95 to 175°C dm^{-1} at the surface. In contrast, south-facing rockwalls revealed higher maximum summed annual temperature gradients between 377°C dm^{-1} (RW1-S) and 816°C dm^{-1} (RW3-S).

4.3. Frost Cracking Model Results

The HR-Model showed the largest intensity of frost cracking between 1.17 and 1.32°C-day dm^{-1} at RW1-S and between 1.53 and 1.71°C-day dm^{-1} at RW3-S at south facing rockwalls (Figures 5a, 5s, and 7e). The frost cracking maximum was located at (0.1 m) or near the surface (0.1–0.3 m). Frost cracking affected the rock mass down to 0.9 and 1.8 m rock depth (Table 4). North-facing rockwalls revealed a decrease of frost cracking and frost penetration depth with increasing altitude (Figures 5g, 5m, 5y, 5ae, and 7e, Table 4). Frost cracking peaks were reached at the surface. The A-Model showed an identical pattern of frost cracking, but

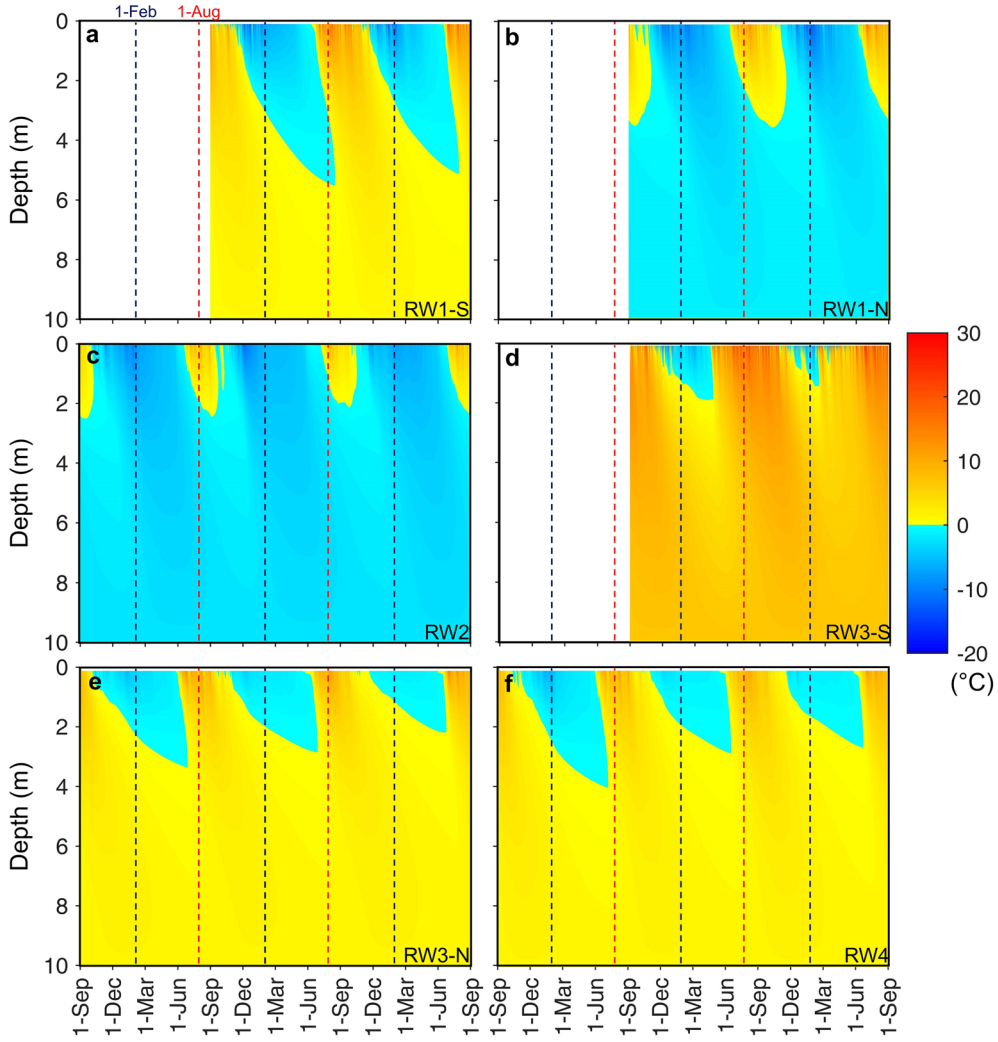

Figure 4. Modeled rock temperature distribution of the upper 10 m depth for the period September 1, 2016 until August 31, 2019. Rockwalls are arranged along the topographical gradient from 3,158 to 2,580 m. Red dotted lines highlight 1st of August and blue dotted lines 1st of February in each year.

Table 4
Maximum Modeled Frost Cracking Intensity (FCI), Depth of Maximum FCI, Depth Range of Frost Cracking for HR-, A-, WH-, and R-Model

	Maximum frost cracking intensity				Depth of maximum FCI (m)				Depth range of frost cracking (m)			
Rockwall	HR (°C-day/dm)	A (°C-day/dm)	WH (m)	R (%)	HR	A	WH	R	HR	A	WH	R
RW1-S	1.17–1.32	0.21–0.32	0.27–0.38	0.07	0.1–0.3	0.1–0.3	0.8–0.9	0.1	0.1–1.8	0.1–1.8	0.1–1.8	0.1–1.0
RW1-N	0.06–0.14	0.03–0.04	0.16–0.17	0.02–0.03	0.1	0.1	0.3–1.1	0.1–0.9	0.1–0.2	0.1–0.2	0.1–3.1	0.1–1.7
RW2	0–0.08	0–0.01	0.11–0.13	0.01–0.02	0.1	0.1	0.2–0.5	0.1–0.3	0–0.4	0–0.4	0.1–2.0	0.1–1.3
RW3-S	1.53–1.71	0.39–0.64	0.11–0.19	0.10–0.15	0.1	0.1	0.1–0.3	0.1	0.1–0.9	0.1–0.9	0.1–1.0	0.1–0.5
RW3-N	0–0.68	0–0.08	0.10–0.11	0	0.1	0.1	0.1	NF	0.1–0.7	0–0.7	0.1–0.4	0
RW4	0.07–0.67	0.01–0.04	0.10–0.19	0–0.01	0.1	0.1	0.1	0.1	0–1.1	0.1–1.1	0.1–1.0	0–0.2

Abbreviation: FCI, Frost cracking intensity; NF, No frost cracking.

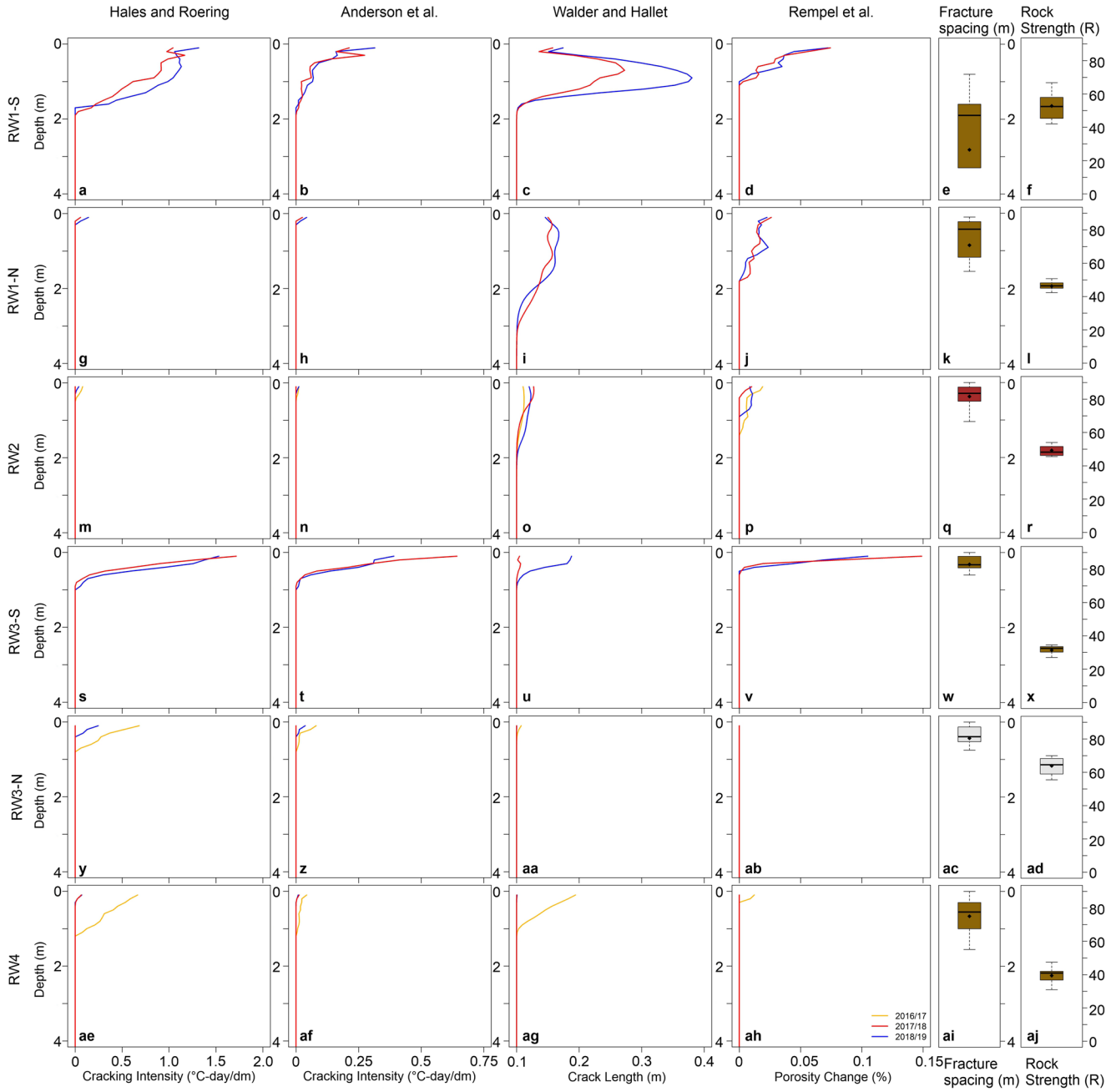

Figure 5. Modeled frost cracking in terms of frost cracking intensity, crack length or porosity change using the models by Hales and Roering (2007), Anderson et al. (2013), Walder and Hallet (1985), and Rempel et al. (2016) plotted versus rock depth. Boxplots of measured fracture spacing and measured rock strength with diamonds presenting mean values. Rockwalls are arranged along the topographical gradient from 3,158 to 2,580 m.

the magnitude of modeled frost cracking was reduced by 65%–80% on south facing rockwalls (Figures 5b and 5t) and by 20%–90% on north facing rockwalls (Figures 5h, 5n, 5z, 5af, and 7f, Table 4).

The WH-Model revealed the highest modeled crack lengths at RW1-S with 0.27–0.38 m and RW1-N with 0.16–0.17 m located at ~3,157 m (Figure 7g). The peak of frost cracking was reached at a depth between 0.8 and 0.9 m on the south-facing rockwall and between 0.3 and 1.1 m on the north-facing rockwall and affected the rockwall up to 1.8 m depth at RW1-S and 3.3 m at RW1-N (Figures 5c and 5i, Table 4). RW2 consisting of aplite and located at 2,907 m showed a lower crack length growth than RW1-N with a peak at 0.2–0.5 m. Frost cracking affected the rockwall to 2 m depth (Figure 5o). The south-facing RW3-S showed crack length

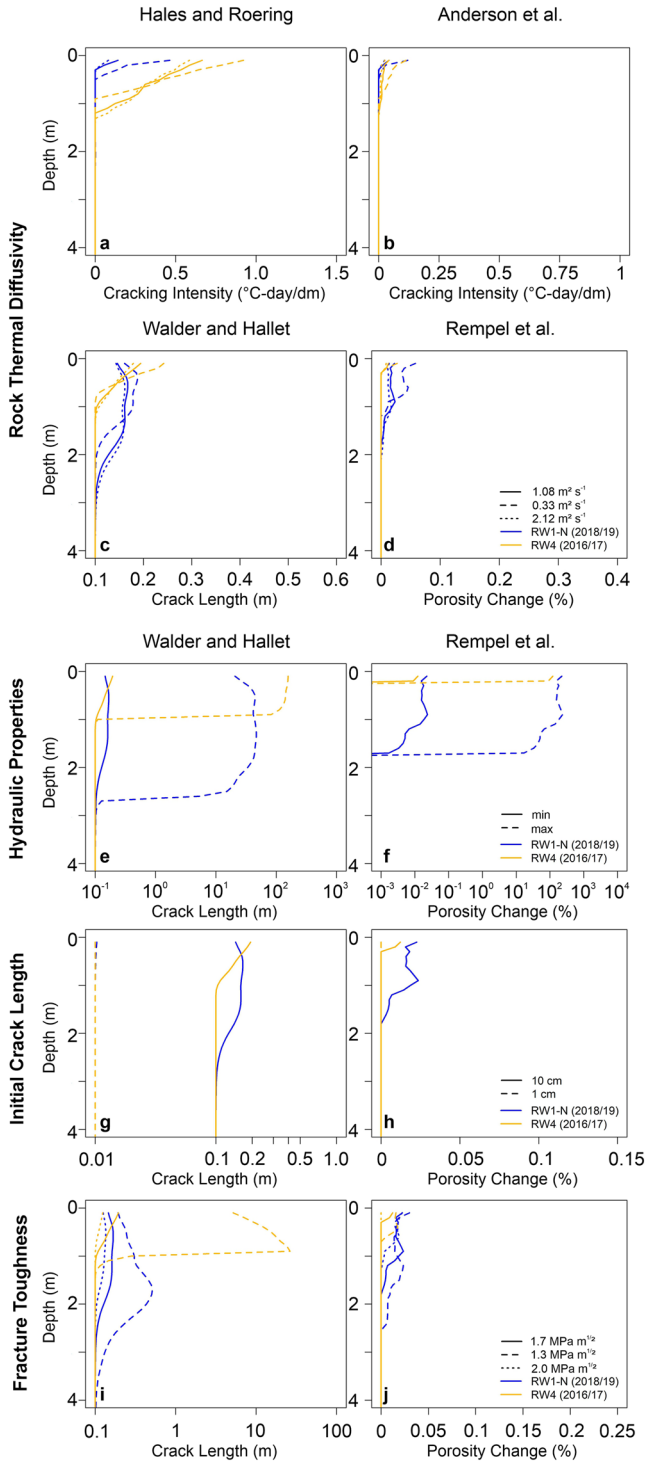

Figure 6. Sensitivity analysis of rock thermal diffusivity for the models by (a) Hales and Roering (2007), (b) Anderson et al. (2013), (c) Walder and Hallet (1985), and (d) Rempel et al. (2016). Sensitivity analysis of (e) hydraulic conductivity and (f) hydraulic permeability, (g–h) initial crack length and (i–j) fracture toughness of the models by Walder and Hallet (1985) and Rempel et al. (2016). Modeled results of logger RW1-N from 2018/19 (blue lines) to RW4 from 2016/17 (yellow lines) are exemplary shown, for a complete sensitivity analysis see Figures S1–S4.

growth up to 0.11 and 0.19 m with high differences between 2017/18 and 2018/19 (Figure 5u). The peak crack length growth was reached at the surface and frost weathering penetrated 1 m into the rock mass. In contrast, RW3-N consisting of amphibolite revealed no to very low crack length growth with a maximum at the surface and a rock mass affected up to 0.4 m depth (Figure 5aa). RW4 showed frost cracking only in 2016/17 and crack length reached 0.19 m with a maximum at the surface and a penetration depth up to 1.1 m (Figure 5ag).

The R-Model revealed a frost cracking pattern similar to the WH-Model (Figure 7h). The highest magnitude of frost cracking was modeled at south-facing rockwalls with a porosity change of 0.1%–0.15% at RW3-S and 0.07% at RW1-S (Figures 5d and 5v, Table 4). The maximum frost cracking was modeled at the surface and affected the rockwalls to a depth of 1 m at RW3-S and 1.8 m at RW1-S. North-facing rockwalls RW1-N and RW2 revealed a porosity change of 0.02%–0.03% with a maximum at the surface but also a second peak between 0.3 and 0.9 m rock depth. Frost cracking affected the rockwalls to depth between 1.3 and 1.7 m (Figures 5j and 5p). RW3-N, consisting of amphibolite, showed no frost cracking at all (Figure 5ab), while frost cracking at RW4 was minimum (0.01%) with a low penetration depth of 0.2 m and the maximum at the surface (Figure 5ah).

4.4. Sensitivity Analysis

We tested the sensitivity of the used frost cracking models for rock thermal diffusivity, hydraulic properties, initial crack length and fracture toughness. Rock thermal conductivity and specific heat capacity varies largely within rock types and we used end members of calculated rock thermal diffusivity. Decreasing the rock diffusivity shifted the modeled frost cracking pattern in all used models. The magnitude of frost cracking was amplified, but the depth at which peak intensity occurred was shifted closer to the surface and the penetration depth was reduced (Figures 6a–6d, Figure S1). Increasing the rock thermal diffusivity resulted in a decrease of frost cracking magnitude, slightly reduced the penetration depth and shifted the frost cracking peak. Increasing the hydraulic conductivity from 5×10^{-14} to 5×10^{-10} m s^{-1} and hydraulic permeability from 10^{-18} to 10^{-14} m^2 increased the frost cracking magnitude of the WH- and R-Model, while penetration depth and peak location was maintained (Figures 6e, 6f, and S2). In WH-Model, the four-order of magnitude increase of hydraulic conductivity resulted in an increase of crack length growth by two to three orders of magnitude. The hydraulic permeability increase by four orders of magnitude shifted the porosity change in the R-Model by the same order of magnitude.

Applying a decreased initial crack length of 0.01 m instead of 0.1 m, the frost cracking was decreased to zero in the WH- and R-Model (Figures 6g, 6h, and S3). Only at RW1-N, the WH-Model showed a minor frost cracking activity. For sensitivity analysis of fracture toughness, we used maximum and minimum end members for each rock type. Increasing the fracture toughness shifted the modeled frost cracking pattern in WH- and R-Model with a reduced magnitude, a peak closer to surface and reduced penetration depth (Figures 6i, 6j, and S4). In contrast, decreasing fracture

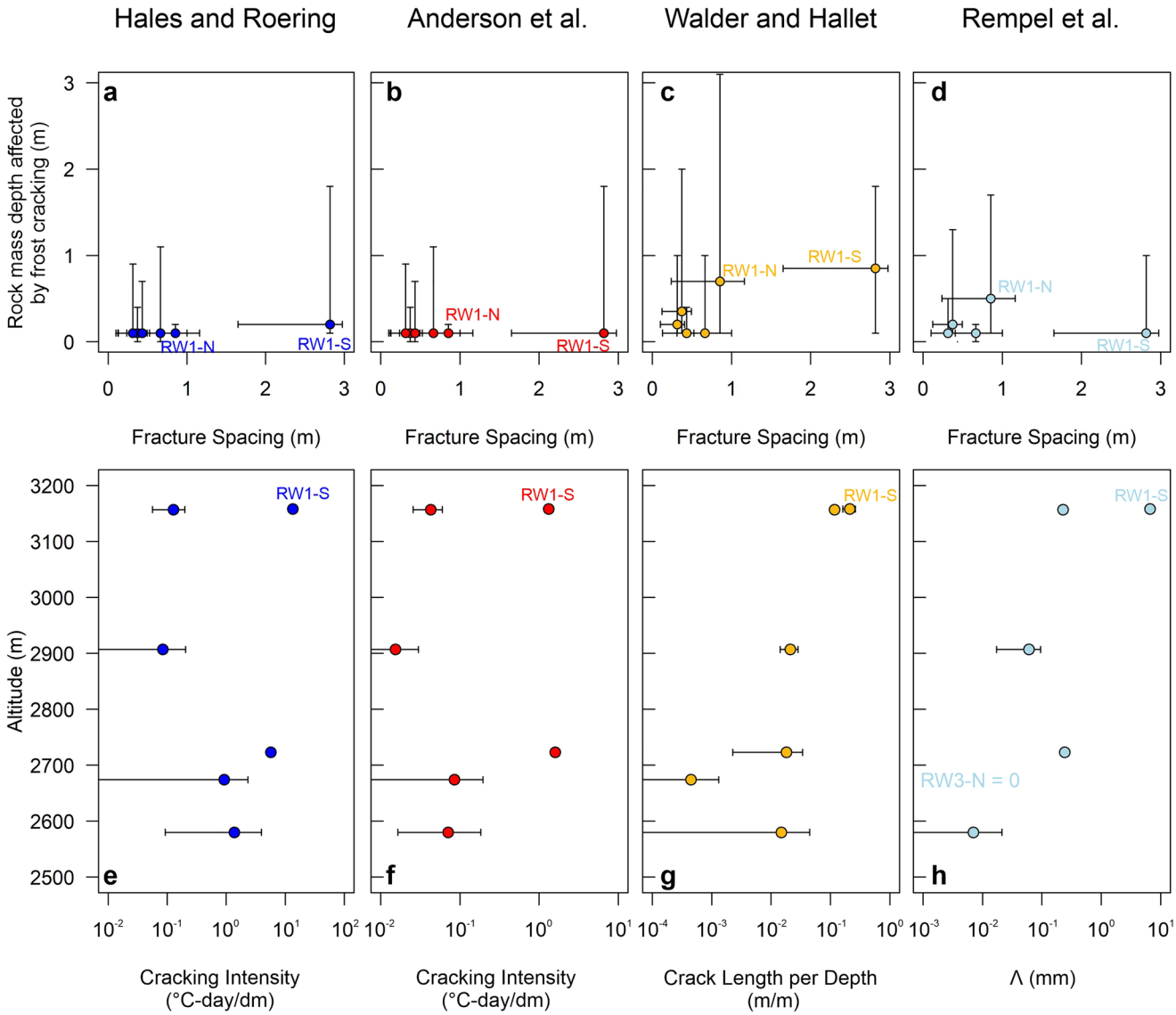

Figure 7. (a–d) Rock mass depth affected by frost cracking plotted versus measured fracture spacing. Points represent depth of the maximum frost cracking (Table 4) plotted versus mean fracture spacing of each rockwall. Error bars indicate the range of modeled frost cracking depth (Table 4) and the lower and upper quartile of measured fracture spacing. Modeled mean cracking intensity of (e) Hales and Roering (2007) and (f) Anderson et al. (2013), (g) modeled depth-integrated crack length using the model by Walder and Hallet (1985), (h) modeled depth-integrated porosity change using the model by Rempel et al. (2016) plotted versus altitude. The error bars present the minimum and maximum modeled frost cracking of each model.

toughness resulted in a frost cracking shift with frost cracking magnitude increase, a peak located at a greater depth and deeper frost cracking penetration (Figures 6i, 6j, and S4).

5. Discussion

5.1. Thermal Regime of the Rockwalls

Air temperatures are influenced by elevation, but RST also depend on topography, snow cover, fracturing and water availability. The model results for north-facing rockwalls demonstrate that MARST, MWRST, and MSRST show no clear altitudinal trend with decreasing temperatures at higher locations, as expected from AT trends (Table 3). In addition, RSTs revealed an annual variation that increased with altitude at north-exposed rockwalls and was amplified at south-facing rockwalls (Figures 3b–3g). RSTs revealed higher temperatures at RW1 than RW2, which we interpret as a result of increased solar radiation on the ridge

(Figure 1b) compared to shaded location at RW2 within the Rothorn cirque (Figure 1c), therefore, the altitudinal pattern is disturbed by shading effects due to topography as previously observed by several studies (e.g., Haberkorn, Hoelzle, et al., 2015). Daily temperature variation increased from north-facing rockwalls with 4°C variation up to 16.5°C at south-exposed rockwalls. We interpret this behavior as a result of topography that changes the insolated geometry and results in solar radiation differences (Gruber et al., 2004; Hasler, Gruber, & Haeberli, 2011).

Our rock temperature data showed 2.2°C–2.5°C warmer MARST at south-facing rockwalls to north-facing rockwalls at RW1, which even increased to 4.6°C–6.0°C at RW3 (Table 3). Rockwalls at RW1 are located on approximately identical elevation, while RW3-S is located 50 m above RW3-N, which corresponds to a 0.3°C temperature decrease based on the calculated lapse rate of 6°C km^{-1}. This would even increase the observed temperature difference. The measured MARST differences are within the range of previously observed aspect-induced differences that ranged between 3.3°C and 3.8°C at Gemsstock (Haberkorn, Hoelzle, et al., 2015), up to 3.9°C at the Steintaelli in 2012–2014 (Draebing, Haberkorn, et al., 2017) and up to 5°C in partly snow covered rockwalls at Aiguille du Midi (Magnin et al., 2015), Matterhorn and Jungfraujoch (Hasler, Gruber, & Haeberli, 2011). Several authors observed also an increase of MARST differences up to 7°C in snow-free rockwalls (Gruber et al., 2004; Hasler, Gruber, & Haeberli, 2011). These large MARST differences results in permafrost occurrence on the north-facing RW1-N, while RW1-S is permafrost-free as demonstrated by geophysical measurements between 2006 and 2019 (Draebing, Haberkorn, et al., 2017; Krautblatter & Draebing, 2014; Scandroglio et al., 2021). Our recorded aspect-induced temperature differences correspond to an altitude between 350 and 1,000 m assuming a temperature lapse rate of 6°C km^{-1} and demonstrate that MAAT adjusted to altitudes will fail completely to simulate the influence of aspect.

Snow cover in rockwalls is highly variable due to topographic effects such as slope angle, distance to rock ledges and wind drift (Haberkorn, Hoelzle, et al., 2015; Wirz et al., 2011). Our logger data revealed a decreased snow duration at RW1-N at 3,157 m (120–161 days) compared to lower-elevated RW2, RW3-N, and RW4 (>207 days; Table 3 and Figure 3). RW1 also experienced a delayed onset of snow cover, which can be the result of less topographic shading and enhanced solar radiation at ridge locations (Haberkorn, Hoelzle, et al., 2015), steeper rockwalls and a longer required snow accumulation time from the below laying ledge slope upwards as observed previously in the Steintaelli (Draebing, Haberkorn, et al., 2017). Less snow cover at RW1-N enabled more cooling in winter (Figure 3c). Our data demonstrated an earlier snow melt at RW1-N compared to RW2-RW4 especially in 2018/19 (Figure 3), which we interpret as a result of increased insolation at the ridge location. At north-facing rockwalls, the thermal offset fluctuated around zero during snow-free periods (Figures 3c, 3d, 3f, and 3g), however, the thermal offset was positive indicating warmer RST than AT following snow onset. This indicates that snow cover had a warming effect on rockwall temperatures (Draebing, Haberkorn, et al., 2017; Luetschg et al., 2008). A delayed snow onset as observed at RW1-N results in increased cooling of the rockwall. The thermal offset reversed to negative temperatures at half or two third of the snow cover period, therefore, RST were colder than ATs and snow had a cooling effect (Draebing, Haberkorn, et al., 2017; Luetschg et al., 2008). In summary, insolation and insulation controls the effect of air on RST. The insulation effect can be decreased in very steep cliffs due to decreased or lack of snow cover. Frost weathering approaches using an elevation-adjusted MAAT with uniform half amplitudes for annual or daily oscillation fail to model the thermal regime adequately (e.g., Delunel et al., 2010; Hales & Roering, 2009; Scherler, 2014). Anderson et al. (2013) already stated that frost cracking models should take the radiation field and non-uniform snow cover more realistically into account, thus, these effects results in complex RST histories. By using measured RST, we are able to integrate these complexities into our frost cracking model approach.

5.2. Sensitivity of Frost Cracking Models to Thermal, Hydraulic, and Mechanical Properties

5.2.1. Influence of Thermal Parameters and Thermal Processes on Frost Cracking

The thermal regime was modeled based on assumptions on heat transport, porosity and water infill, which vary spatially and temporally and cannot be better resolved by existing model approaches. The investigated rockwalls comprising schisty quartz slate are highly anisotropic resulting from rock fabric (anisotropy factor 0.55) compared to isotropic amphibolite (0.05) and aplite (0.06) (Draebing & Krautblatter, 2019). However, the heat transport model assumes an isotropic rock. The rock mass of rockwalls comprise fractures,

which are incorporated into the heat transport model by increasing porosity from below 1% to 3% (Table 2), which is the common way to incorporate fractures in conductive heat models (Noetzli & Gruber, 2009; Noetzli et al., 2007; Wegmann, 1998). An increased water-filled porosity will significantly increase the lag of heat transport due to latent heat processes (Wegmann, 1998). In addition, fractures increase vertical groundwater flow (Dietrich et al., 2005; Forster & Smith, 1989) and associated advective heat transport (Draebing et al., 2014; Gruber & Haeberli, 2007) as well as convective heat transport by wind (Gischig et al., 2011a, 2011b; Moore et al., 2011), which are neglected in the conductive heat transport model. Therefore, the application of heat transport models to anisotropic rocks and rock masses can result in over- or underestimation of rock temperatures. In high-Alpine rockwalls, heat transport is affected by topography and heat transport from warmer south to colder north rockwalls (Noetzli et al., 2007). These 3D-effects can be incorporated on individual mountain peaks, but these processes cannot be resolved by 1D-model approaches or incorporated to frost weathering models working on larger geomorphic scales as landscapes (e.g., Hales & Roering, 2007; Rempel et al., 2016).

Rock thermal diffusivity varies within rock types and between rockwalls. To test the influence of thermal diffusivity on frost cracking, we applied a wide range of diffusivities to frost cracking modeling. All frost cracking models showed a sensitivity to thermal diffusivity but the magnitude and depth of the frost cracking pattern is persistent between different diffusivities. Decreasing the thermal diffusivity increased the frost cracking magnitude but decreased the penetration depth (Figures 6a–6d and S1). In contrast, an increased diffusivity decreased the frost cracking magnitude but increased the affected depth within the rock mass. All models used a temperature gradient in their frost cracking simulation. Our data revealed that maximum summed temperature gradients at the surface of south-facing rockwalls were between 372°C dm^{-1} (RW1-S) and 816°C dm^{-1} (RW3-S) and more than two times larger than temperature gradients at north-facing rockwalls, which ranged from 95°C to 175°C dm^{-1}. Higher temperature gradients result in higher FCI for the HR- and A-Model (Anderson et al., 2013; Hales & Roering, 2007). In the WH-Model, increased temperature gradients amplify water migration toward the freezing front by decreasing flow resistance (see Equation A-2 in Walder & Hallet, 1985). Therefore, ice lenses growth is amplified and can develop higher ice pressures. In the R-Model, the square of the temperature gradient is used to calculate the porosity change (see Equation 7 in Rempel et al., 2016), and so the influence of conductivity is increased in this model. In summary, the dependence on temperature gradient explains the higher FCI in all models at south-facing rockwalls (Figures 5 and 7e–7h). The range of thermal regime, where frost cracking occurs, plays a major control on the frost weathering model. The HR- and A-Model apply a strict temperature range called FCW between −8°C and −3°C. This range corresponds with laboratory measurements of frost cracking on high porosity Berea sandstone (Hallet et al., 1991), but laboratory and field measurements of acoustic emissions demonstrated that frost cracking occurred as soon as alpine rocks froze (Amitrano et al., 2012; Duca et al., 2014; Girard et al., 2013). Field measurements also observed frost cracking occurring at temperatures down to −15° (Amitrano et al., 2012; Girard et al., 2013) and no temperature cut off. In contrast, the WH- and R-Model incorporate hydraulic and mechanical factors into their models that control the temperature limits of frost cracking.

5.2.2. Influence of Water Availability on Frost Cracking

The occurrence of water is a prerequisite for frost weathering and all used models assume saturated conditions. Rock moisture measurements in intact rock showed that rocks are not fully saturated and moisture fluctuates in the upper 0.2 m during the year (Girard et al., 2013; Sass, 2005a). The moisture fluctuation is influenced by moisture percolation through the fracture network (Dietrich et al., 2005; Forster & Smith, 1989; Girard et al., 2013) and by distance to snow fields that contribute moisture during snow melt (Girard et al., 2013; Sass, 2005a). Moisture simulations suggest that slope angle and lithology can cause differences in pore water saturation (Rode et al., 2016). Therefore, results from all frost cracking models represent the maximum scenario of frost cracking. Fractures increase not only permeability of rocks and access of water, but enhance chemical and biological activity in the subsurface, which can weaken rock and therefore amplify further cracking (Anderson et al., 2013).

The HR-Model assumes the availability of water from the surface or from groundwater in 20 m depth (in our model 10 m depth), when rock temperatures are positive. Therefore, our model results showed lowest frost cracking activity in permafrost affected rockwalls (RW1-N and RW2, Figures 5g and 5m), where rock

temperatures at 10 m are negative throughout the year (Figures 4b–4c). Our model results using the A-Model revealed 65%–80% lower frost cracking activity in south-facing rockwalls and slightly lower frost cracking at north-facing rockwalls. The model assumes water available along rock depths with positive temperatures, however, penalizes water transport, which reduces the frost cracking activity. Anderson et al. (2013) stated that penalization is a simplification and not a true assessment of water availability. Water in rock can be present even in frozen rocks (Mellor, 1970), but the water preconditions of the A-Model resulted in low or no frost cracking at permafrost affected rockwalls RW1-N and RW-2 (Figures 5h and 5n).

The WH- and R-Model assume saturated conditions but use hydraulic conductivity or permeability at the pore freezing point to reduce water availability. Unfrozen permeability varies by six orders of magnitude (Rempel et al., 2016) and applying a sensitivity test of hydraulic permeability and conductivity with end members differing by four orders of magnitude demonstrate a high sensitivity of both models. The frost cracking magnitude increased between two and three orders in the WH- and four orders in the R-Model (Figures 6e, 6f and S2), though the depth and location of magnitude pattern is persistent. Therefore, the magnitude of frost cracking can only be interpreted in a qualitative way, but the depth pattern can be quantitatively compared to fracture spacing and rock strength. Hydraulic properties are affected by curvature effects and influenced by pore size, grain size and ice-liquid surface energy, which are poorly constrained and vary at geomorphic scales such as rockwalls. Our model results of WH- and R-Models revealed intense frost cracking in the permafrost-affected rockwalls RW1-N and RW2 (Figures 5i, 5j, 5o, and 5p). Murton et al. (2006) used the model by Walder and Hallet (1985) to model frost cracking in high porosity and isotropic permafrost-affected Tuffeau limestone samples and the modeled cracking lengths reflected well observed crack clustering. Walder and Hallet (1985) use a generalized Darcy's law with a constant hydraulic conductivity k_{hc} of 5×10^{-14} m s^{-1} based on sediments and soils. In contrast, Rempel et al. (2016) determine their lower boundary of frost cracking by integrating permeability in the form of a simple power-law approximation. Both approaches result in frost cracking activity in temperature ranges from −1°C down to −15°C, which are in better accordance to field measurements (Amitrano et al., 2012; Girard et al., 2013).

5.2.3. Influence of Initial Crack Length and Fracture Toughness

The problem of cracking is associated with initial conditions associated with rock structure (Anderson et al., 2013). Cracks can be generated by tectonic stress (Molnar et al., 2007), paraglacial stress release (Grämiger et al., 2017; Grämiger et al., 2020), and internal stress distribution (Leith et al., 2014a, 2014b) following glacier retreat or surface processes (Clarke & Burbank, 2010, 2011). Cracks also develop progressively (Walder & Hallet, 1985) and therefore initial conditions will be far away from assumed constant cracks. The WH- and R-Models are sensitive to initial crack length. Decreasing crack length by one order of magnitude reduced frost cracking to zero or leads to almost no frost cracking at RW1-N (Figures 6g, 6h, and S3).

The WH- and R-Models are sensitive to fracture toughness as our model results demonstrated a decrease of frost cracking magnitude with a peak closer to the surface and reduced penetration depth as fracture toughness increases (Figures 6i, 6j, and S4). In contrast, decreasing fracture toughness increased the frost cracking magnitude, shifted the peak to higher depth and increased penetration depth. Walder and Hallet (1985) incorporate fracture toughness by increasing the length of penny-shaped cracks when ice pressure reached a third of fracture toughness. Since frost cracking starts as ice pressure approaches the rock strength and ice pressure development depends on temperature, each rock type has an individual strength-dependent frost cracking temperature range (Walder & Hallet, 1985), which is supported by laboratory and field studies (Draebing & Krautblatter, 2019; Draebing, Krautblatter, & Hoffmann, 2017; Murton et al., 2006). Therefore, frost cracking is enhanced at RW1-N, RW1-S, RW3-S and RW-4 (Figures 5c, 5d, 5i, 5j, 5u, 5v, 5ag, and 5ah), where low-strength schisty quartz slate (fracture toughness 1.66 MPa $m^{1/2}$) is abundant, in contrast to higher strength aplite (1.87 MPa $m^{1/2}$) at RW2 (Figures 5o and 5p) and amphibolite (2.19 MPa $m^{1/2}$) at RW3-N (Figures 5aa and 5ab).

The upper boundary of the R-Model is calculated based on fracture toughness and crack length. This upper temperature limit of frost cracking increases from amphibolite to aplite and schisty quartz slate due to decreasing K_C and increases with increasing crack length (Figure S5). Therefore, large cracks are more easily propagated than small cracks, which is in accordance to studies on fracture mechanics (Atkinson & Rawlings, 1981; Erismann & Abele, 2001). A uniform crack length is assumed during modeling and frost weathering is expressed as porosity increase, therefore, a progressive fracture propagation with time that

increases effective porosity and enhances fluid flow is ignored. Due to higher strength of amphibolite, no frost cracking occurs at all at RW3-N, while lower strength schisty quartz slate rocks are easier to crack.

5.3. Topographic Pattern of Frost Cracking in the Hungerli Valley

All models showed highest frost cracking activity at south-facing rockwalls, but the fracture spacing and rock strength measurements cannot support the resulting frost cracking patterns. The highest overall frost cracking was measured at RW1-S and affected the upper 1 m in the R-Model and upper 1.8 m in the HR-, A-, and WH-Models (Figures 5a–5d). However, fracture spacing showed variation between 1.65 and 2.98 m with an average spacing of 2.82 m (Figure 5e); therefore, fracture spacing is larger than the effect of frost cracking within the rock mass and does not correspond to the model results (Figures 7a–7d). With the exception of the WH-Model, all models revealed a peak frost cracking at the surface. Repetitive frost cracking activity reduces both compressive and tensile strength of rocks (Jia et al., 2021, 2015); therefore, a frost cracking peak at the surface should result in lowering the rock strength due to rock breakdown. However, Schmidt hammer measurements at RW1-S showed the highest measured rebound values (53) of schisty quartz slate rocks (Figure 5f), which is contrary to the modeled frost cracking patterns. The rebound value could be increased if fresh rock is exposed following a rockfall, but a fresh rockfall scar was not visible at RW1-S or any other logger location.

Model results from RW3-S showed high frost cracking rates (Figures 7e–7h) with an affected rock mass of 0.5 m in the R-Model, 0.9 m in HR- and A-Models and 1 m in the WH-Model (Figures 5s–5v). Fracture spacing varied between 0.1 and 0.41 m with a mean of 0.32 m (Figure 5w) which corresponds best with the R-Model. Frost cracking showed highest magnitudes at surface at all models and mean rebound values were the lowest measured values in the Hungerli Valley (31). The Schmidt hammer value corresponds to a high weathering activity at the surface (Figure 5x). However, measured fracture spacing is smaller than the rock mass affected by frost cracking activity, therefore, other weathering processes affecting the near surface of rockwalls can be responsible for near surface cracking. RW3-S experienced highest daily thermal variation, which can increase thermal stresses (Eppes et al., 2016) that can support near surface rock breakdown and, therefore, the low rock strength can be a result of other weathering processes than frost weathering. Field observations using rockfall collectors and talus deposits recorded significantly more frost weathering associated rockfall at north-facing than south-facing rockwalls (Sass, 2005b, 2007), but frost cracking models in this study revealed highest magnitudes at south-facing rockwalls. The contrary model patterns of RW1-S and RW3-S can be a result of unrealistic rock moisture assumptions at south-facing rockwalls. Due to higher insolation, south-facing rockwalls have the lower moisture contents near to the surface (0.2 m; Rode et al., 2016; Sass, 2005a) where highest frost cracking magnitudes were modeled. Therefore, moisture conditions are contrary to assumed saturated conditions in the frost cracking model set up. However, there is no study yet that provides information on aspect-induced rock moisture variation below 0.2 m, which would enable an improvement of used model assumptions.

The permafrost affected rockwalls RW1-N and RW2 showed contrary results between purely thermal models (HR and A-Model) and thermo-mechanical models (WH- and R-Model; Figures 7e–7h). At RW1-N, frost cracking effects were limited to the upper 0.1–0.2 m of the rockwall in the HR- and A-Model with peaks at the surface (Figures 5g, 5h, 5m, and 5n). We interpret this frost cracking pattern as a result from the water availability assumptions (see Section 5.2.2). In contrast, WH- and R-Models revealed high frost cracking intensities. The WH-Model showed an affected rock mass of 3.1 m with peak intensity at 0.3–1.1 m (Figure 5i), while the R-Model revealed a penetration depth of 1.7 m with peaks between 0.1 and 0.9 m (Figure 5j). These model results correspond to measured fracture spacing that ranged between 0.24 and 1.16 m with an average of 0.85 m (Figures 5k, 7c, and 7d). Schmidt hammer values at RW1-N were 46 and suggest a hard rock strength due to low FCI at the surface (Figure 5l). RW2 showed a similar pattern with decreased penetration depth to 1.3 m in the R-Model (Figure 5p) and 2 m in the WH-Model (Figure 5o) and peaks at 0.1–0.3 m and 0.2–0.5 m, respectively. Model results correspond to measured fracture spacing that varied between 0.12 and 0.5 m with an average of 0.37 m (Figure 5q). Rebound values of the aplite rockwall were 40 (Figure 5r), which suggests less frost cracking at the surface and corresponds better with WH-Model results.

RW3-N consists of high-strength amphibolite characterized by high rebound values of 64 (Figure 5ad). The R-Model showed no frost cracking and WH-Model only minor frost cracking limited to the upper 0.4 m in

2016/17 (Figures 5aa and 5ab), which we interpret as a result of insufficient ice pressure development that were unable to exceed the rock strength thresholds of the models. In contrast, the A-Model showed highest frost cracking on north-facing rockwalls and the HR-Model slightly lower magnitudes (Figures 5y, 5z, 7e, and 7f). FCI peaked at the surface and reached to 0.7 m. Fracture spacing ranged from 0.13 to 0.52 m with a mean spacing of 0.43 m (Figure 5ac) that corresponds with HR-, A- and WH-Model results (Figures 7a–7c). However, the observed peaks at the surface especially of the A- and HR-Model are contrasting to the highest measured rebound values of 64 (Figure 5ad). RW4 consisting of schisty quartz slate showed highest frost cracking intensities at HR- and WH-Models and lower intensities at A- and R-Models (Figures 5ae–5ah). Fracture spacing ranged from 0.21 to 1 m with 0.67 m on average (Figure 5ai), which corresponds better to A-, HR-, and WH-Models (Table 4) than the R-Model that showed only minor penetration depth of 0.2 m. The low measured rebound value of 39 (Figure 5aj) supports the occurrence of high intensities at surface simulated by all models.

Anomalous high frost cracking intensities on south-facing rockwalls resulted from model limitations and therefore we excluded these rockwalls from the following analysis. The north-facing rockwalls in the Hungerli Valley experience a topographic pattern of frost cracking with increasing frost cracking with decreasing altitude in the HR- and A-Models and a contrary increasing frost cracking activity with increasing altitude in the WH- and R-Models (Figures 7e–7h). Fracture spacing (Figures 7a–7d) and Schmidt hammer values suggest a higher correspondence of results obtained using WH- and R-Models. In the calcareous Alps, field observations recorded an increased rockfall activity at higher location using rockfall collectors (Sass, 2005b) and using lichenometry on talus slopes (Sass, 2010). Sass (2005b, 2010) suggested that the observed rockfall increase along altitude was associated with permafrost increased frost weathering. Therefore, field studies contradict model results by HR- and A-model and support the observed frost cracking patterns of the WH- and R-Models. Frost weathering is increased at high elevations, increases rockwall erosion and on long-term scale could limit mountain height by acting as a frost buzzsaw (Hales & Roering, 2009). Warming by climate change will reduce frost cracking at our observed rockwalls. Other weathering processes such as thermal (e.g., Eppes et al., 2020), chemical (Murphy et al., 2016) or biological weathering (Viles, 2013) could become more important controls on rockwall erosion. In Alpine environments, the thermal regimes enhancing frost cracking will be shifted to higher elevations which can alter rockwall erosion as well as rockfall and debris flow hazard potential.

6. Conclusions

In high Alpine rockwalls, topography controls the thermal regime by changing insolation and insulation. Consequently, a thermal offset between AT and RST exists; this complicates an AT based frost cracking model approach. Frost weathering depends on the thermal regime, water availability and mechanical rock properties. Our sensitivity analysis demonstrated that thermo-mechanical models are very sensitive to hydraulic parameters and frost cracking changes by orders of magnitude, while the models are less sensitive to mechanical and thermal parameters. As a result of the sensitivity, the predictions of frost cracking magnitude changes, but the spatial frost cracking patterns within the rock mass including the peak locations are consistent. All frost cracking models indicated that the highest modeled frost weathering occurs on south-facing rockwalls, which is contrary to measured fracture and rock strength properties of these rockwalls and to results of previous field studies. We suggest that this is a result of overestimated rock moisture availability, which would reduce frost weathering and should be investigated in future research. Purely thermal models underestimate the FCI in permafrost-affected rockwalls due to their water-availability constraints. In contrast, thermo-mechanical models incorporate hydraulic permeability or conductivity and show the highest frost cracking in permafrost-affected rockwalls, which is consistent with observed fracture and rock strength patterns. Thermo-mechanical models revealed a topographic altitudinal frost cracking pattern characterized by an increasing frost weathering intensity with increasing altitude, while purely thermal models showed an inverse related topographic frost cracking pattern with highest intensities at lower elevations. Therefore, thermo-mechanical models produced more realistic frost weathering patterns on rockwalls and along topographic gradients in the Hungerli Valley. According to the model results of thermo-mechanical frost cracking models, climate change induced warming will reduce frost cracking at

our observed rockwalls. In Alpine environments, thermal regimes enhancing frost cracking will be shifted to higher elevations, which will affect rockwall erosion and hazard potential.

Data Availability Statement

All datasets for this research are available at doi: 10.6084/m9.figshare.14178539.

Acknowledgments
Daniel Draebing received funding from the German Research Foundation (DR1070/1-1 and DR1070/3-1). The authors thank Arne Thiemann, Arne Brandschwede, Florian Strohmaier and Sam McColl for fieldwork support. The authors acknowledge laboratory support at Technical University of Munich by Fritz Ettl, Heiko Käsling, and Georg Stockinger. The authors thank the editor Amy East, associate editor Matthew Brain, Jill Marshall, and two anonymous reviewers for their comments that helped to significantly improve the manuscript. Furthermore, Daniel Draebing thanks Michael Krautblatter and Maarten Kleinhans for hospitality. Open access funding enabled and organized by Projekt DEAL.

References

Amitrano, D., Gruber, S., & Girard, L. (2012). Evidence of frost-cracking inferred from acoustic emissions in a high-alpine rock-wall. *Earth and Planetary Science Letters*, *341–344*, 86–93. https://doi.org/10.1016/j.epsl.2012.06.014

Andersland, O. B., & Ladanyi, B. (2004). *Frozen ground engineering*. Hoboken: John Wiley & Sons.

Anderson, R. S. (1998). Near-surface thermal profiles in alpine bedrock: Implications for the frost weathering of rock. *Arctic and Alpine Research*, *30*(4), 362–372. https://doi.org/10.2307/1552008

Anderson, R. S., Anderson, S. P., & Tucker, G. E. (2013). Rock damage and regolith transport by frost: An example of climate modulation of the geomorphology of the critical zone. *Earth Surface Processes and Landforms*, *38*(3), 299–316. https://doi.org/10.1002/esp.3330

Atkinson, B. K. (1984). Subcritical crack growth in geological materials. *Journal of Geophysical Research*, *89*(B6), 4077–4114. https://doi.org/10.1029/JB089iB06p04077

Atkinson, B. K., & Rawlings, R. D. (1981). Acoustic emission during stress corrosion cracking in rocks. In D. W. Simpson, & P. G. Richards (Eds.), Earthquake prediction (pp. 605–616). https://doi.org/10.1029/ME004p0605

Bearth, P. (1980). *Geologischer atlas der Schweiz 1:25000. Erläuterungen zum atlasblatt 71 (1308 St. Niklaus)*. Basel: Schweizer Geologische Kommission.

Carslaw, H. S., & Jaeger, J. C. (1986). Conduction of heat in solids (2nd Ed). Oxford: Clarendon Press.

Cermák, V., & Rybach, L. (1982). Thermal conductivity and specific heat of minerals and rocks. In G. Angeneister (Ed.), Landolt–Börnstein Zahlenwerte and Funktionen aus Naturwissenschaften und Technik, Neue Serie, Physikalische Eigenschaften der Gesteine (V/1a) (pp. 305–343), Berlin: Springer.

Chang, S.-H., Lee, C.-I., & Jeon, S. (2002). Measurement of rock fracture toughness under modes I and II and mixed-mode conditions by using disc-type specimens. *Engineering Geology*, *66*(1–2), 79–97. https://doi.org/10.1016/S0013-7952(02)00033-9

Clarke, B. A., & Burbank, D. W. (2010). Bedrock fracturing, threshold hillslopes, and limits to the magnitude of bedrock landslides. *Earth and Planetary Science Letters*, *297*(3–4), 577–586. https://doi.org/10.1016/j.epsl.2010.07.011

Clarke, B. A., & Burbank, D. W. (2011). Quantifying bedrock-fracture patterns within the shallow subsurface: Implications for rock mass strength, bedrock landslides, and erodibility. *Journal of Geophysical Research*, *116*, F04009. https://doi.org/10.1029/2011jf001987

Delunel, R., van der Beek, P. A., Carcaillet, J., Bourlès, D. L., & Valla, P. G. (2010). Frost-cracking control on catchment denudation rates: Insights from in situ produced 10Be concentrations in stream sediments (Ecrins-Pelvoux massif, French Western Alps). *Earth and Planetary Science Letters*, *293*(1–2), 72–83. https://doi.org/10.1016/j.epsl.2010.02.020

Dietrich, P., Helmig, R., Sauter, M., Hötzl, H., Köngeter, J., & Teutsch, G. (2005). *Flow and transport in fractured porous media*. Berlin: Springer.

Dietze, M., Turowski, J. M., Cook, K. L., & Hovius, N. (2017). Spatiotemporal patterns, triggers and anatomies of seismically detected rockfalls. *Earth Surface Dynamics*, *5*(4), 757–779. https://doi.org/10.5194/esurf-5-757-2017

Draebing, D., Haberkorn, A., Krautblatter, M., Kenner, R., & Phillips, M. (2017). Thermal and mechanical responses resulting from spatial and temporal snow cover variability in permafrost rock slopes, steintaelli, swiss alps. *Permafrost and Periglacial Processes*, *28*(1), 140–157. https://doi.org/10.1002/ppp.1921

Draebing, D., & Krautblatter, M. (2012). P-wave velocity changes in freezing hard low-porosity rocks: A laboratory-based time-average model. *The Cryosphere*, *6*, 1163–1174. https://doi.org/10.5194/tc-6-1163-2012

Draebing, D., & Krautblatter, M. (2019). The efficacy of frost weathering processes in Alpine rockwalls. *Geophysical Research Letters*, *46*(12), 6516–6524. https://doi.org/10.1029/2019gl081981

Draebing, D., Krautblatter, M., & Dikau, R. (2014). Interaction of thermal and mechanical processes in steep permafrost rock walls: A conceptual approach. *Geomorphology*, *226*, 226–235. https://doi.org/10.1016/j.geomorph.2014.08.009

Draebing, D., Krautblatter, M., & Hoffmann, T. (2017). Thermo-cryogenic controls of fracture kinematics in permafrost rockwalls. *Geophysical Research Letters*, *44*(8), 3535–3544. https://doi.org/10.1002/2016GL072050

Duca, S., Occhiena, C., Mattone, M., Sambuelli, L., & Scavia, C. (2014). Feasibility of ice segregation location by acoustic emission detection: A laboratory test in Gneiss. *Permafrost and Periglacial Processes*, *25*(3), 208–219. https://doi.org/10.1002/ppp.1814

Eppes, M.-C., & Keanini, R. (2017). Mechanical weathering and rock erosion by climate-dependent subcritical cracking. *Reviews of Geophysics*, *55*(2), 470–508. https://doi.org/10.1002/2017RG000557

Eppes, M. C., Magi, B., Hallet, B., Delmelle, E., Mackenzie-Helnwein, P., Warren, K., & Swami, S. (2016). Deciphering the role of solar-induced thermal stresses in rock weathering. *Geological Society of America Bulletin*, *128*(9–10), 1315–1338. https://doi.org/10.1130/b31422.1

Eppes, M. C., Magi, B., Scheff, J., Warren, K., Ching, S., & Feng, T. (2020). Warmer, wetter climates accelerate mechanical weathering in field data, independent of stress-loading. *Geophysical Research Letters*, *47*(24), 2020GL089062. https://doi.org/10.1029/2020GL089062

Erismann, T. H., & Abele, G. (2001). *Dynamics of rockslides and rockfalls*. Heidelberg: Springer. https://doi.org/10.1007/978-3-662-04639-5

Evans, S. G., & Hungr, O. (1993). The assessment of rockfall hazard at the base of talus slopes. *Canadian Geotechnical Journal*, *30*(4), 620–636. https://doi.org/10.1139/t93-054

Fahey, B. D., & Lefebure, T. H. (1988). The freeze-thaw weathering regime at a section of the Niagara escarpment on the Bruce Peninsula, Southern Ontario, Canada. *Earth Surface Processes and Landforms*, *13*(4), 293–304. https://doi.org/10.1002/esp.3290130403

Forster, C., & Smith, L. (1989). The influence of groundwater flow on thermal regimes in mountainous terrain: A model study. *Journal of Geophysical Research*, *94*(B7), 9439–9451. https://doi.org/10.1029/JB094iB07p09439

Gilpin, R. R. (1979). A model of the "liquid-like" layer between ice and a substrate with applications to wire regelation and particle migration. *Journal of Colloid and Interface Science*, *68*(2), 235–251. https://doi.org/10.1016/0021-9797(79)90277-7

Gilpin, R. R. (1980). Theoretical studies of particle engulfment. *Journal of Colloid and Interface Science*, *74*(1), 44–63. https://doi.org/10.1016/0021-9797(80)90169-1

Girard, L., Gruber, S., Weber, S., & Beutel, J. (2013). Environmental controls of frost cracking revealed through in situ acoustic emission measurements in steep bedrock. *Geophysical Research Letters*, *40*(9), 1748–1753. https://doi.org/10.1002/grl.50384

Gischig, V. S., Moore, J. R., Evans, K. F., Amann, F., & Loew, S. (2011a). Thermomechanical forcing of deep rock slope deformation: 1. Conceptual study of a simplified slope. *Journal of Geophysical Research*, *116*, F04010. https://doi.org/10.1029/2011jf002006

Gischig, V. S., Moore, J. R., Evans, K. F., Amann, F., & Loew, S. (2011b). Thermomechanical forcing of deep rock slope deformation: 2. The Randa rock slope instability. *Journal of Geophysical Research*, *116*, F04011. https://doi.org/10.1029/2011jf002007

Grämiger, L. M., Moore, J. R., Gischig, V. S., Ivy-Ochs, S., & Loew, S. (2017). Beyond debuttressing: Mechanics of paraglacial rock slope damage during repeat glacial cycles. *Journal of Geophysical Research: Earth Surface*, *122*(4), 1004–1036. https://doi.org/10.1002/2016JF003967

Grämiger, L. M., Moore, J. R., Gischig, V. S., Loew, S., Funk, M., & Limpach, P. (2020). Hydromechanical rock slope damage during Late Pleistocene and Holocene glacial cycles in an Alpine valley. *Journal of Geophysical Research: Earth Surface*, *125*, e2019JF005494. https://doi.org/10.1029/2019jf005494

Gruber, S., & Haeberli, W. (2007). Permafrost in steep bedrock slopes and its temperature-related destabilization following climate change. *Journal of Geophysical Research*, *112*, F02S18. https://doi.org/10.1029/2006JF000547

Gruber, S., Hoelzle, M., & Haeberli, W. (2004). Rock-wall temperatures in the Alps: Modeling their topographic distribution and regional differences. *Permafrost and Periglacial Processes*, *15*, 299–307. https://doi.org/10.1002/ppp.501

Haberkorn, A., Hoelzle, M., Phillips, M., & Kenner, R. (2015). Snow as a driving factor of rock surface temperatures in steep rough rock walls. *Cold Regions Science and Technology*, *118*, 64–75. https://doi.org/10.1016/j.coldregions.2015.06.013

Haberkorn, A., Phillips, M., Kenner, R., Rhyner, H., Bavay, M., Galos, S. P., & Hoelzle, M. (2015). Thermal regime of rock and its relation to snow cover in steep alpine rock walls: Gemsstock, Central Swiss Alps. *Geografiska Annaler - Series A: Physical Geography*, *97*(3), 579–597. https://doi.org/10.1111/geoa.12101

Haberkorn, A., Wever, N., Hoelzle, M., Phillips, M., Kenner, R., Bavay, M., & Lehning, M. (2017). Distributed snow and rock temperature modeling in steep rock walls using Alpine3D. *Cryosphere*, *11*(1), 585–607. https://doi.org/10.5194/tc-11-585-2017

Hales, T. C., & Roering, J. J. (2005). Climate-controlled variations in scree production, Southern Alps, New Zealand. *Geology*, *33*(9), 701–704. https://doi.org/10.1130/g21528.1

Hales, T. C., & Roering, J. J. (2007). Climatic controls on frost cracking and implications for the evolution of bedrock landscapes. *Journal of Geophysical Research*, *112*, F02033. https://doi.org/10.1029/2006jf000616

Hales, T. C., & Roering, J. J. (2009). A frost "buzzsaw" mechanism for erosion of the eastern Southern Alps, New Zealand. *Geomorphology*, *107*(3–4), 241–253. https://doi.org/10.1016/j.geomorph.2008.12.012

Halla, C. (2013). *Bewegungsprozesse im Festgestein des Periglazials im Steintälli, Mattertal, Schweiz.* Diploma Thesis, unpublished. Universität Bonn.

Hallet, B., Walder, J. S., & Stubbs, C. W. (1991). Weathering by segregation ice growth in microcracks at sustained subzero temperatures: Verification from an experimental study using acoustic emissions. *Permafrost and Periglacial Processes*, *2*(4), 283–300. https://doi.org/10.1002/ppp.3430020404

Hasler, A., Gruber, S., Font, M., & Dubois, A. (2011). Advective heat transport in frozen rock clefts: Conceptual model, laboratory experiments and numerical simulation. *Permafrost and Periglacial Processes*, *22*(4), 378–389. https://doi.org/10.1002/ppp.737

Hasler, A., Gruber, S., & Haeberli, W. (2011). Temperature variability and offset in steep alpine rock and ice faces. *The Cryosphere*, *5*(4), 977–988. https://doi.org/10.5194/tc-5-977-2011

Hipp, T., Etzelmüller, B., & Westermann, S. (2014). Permafrost in Alpine rock faces from Jotunheimen and Hurrungane, Southern Norway. *Permafrost and Periglacial Processes*, *25*(1), 1–13. https://doi.org/10.1002/ppp.1799

Hirschberg, J., Fatichi, S., Bennett, G. L., McArdell, B. W., Peleg, N., Lane, S. N., et al. (2021). Climate change impacts on sediment yield and debris-flow activity in an Alpine Catchment. *Journal of Geophysical Research: Earth Surface*, *126*(1), e2020JF005739. https://doi.org/10.1029/2020JF005739

ISRM. (1978). Suggested methods for the quantitative description of discontinuities in rock masses. *International Journal of Rock Mechanics and Mining Science & Geomechanics Abstracts*, *15*, 319–368

Jia, H., Ding, S., Zi, F., Li, G., & Yao, Y. (2021). Development of anisotropy in sandstone subjected to repeated frost action. *Rock Mechanics and Rock Engineering*, *54*, 1863–1874. https://doi.org/10.1007/s00603-020-02343-5

Jia, H., Xiang, W., & Krautblatter, M. (2015). Quantifying rock fatigue and decreasing compressive and tensile strength after repeated freeze-thaw cycles. *Permafrost and Periglacial Processes*, *26*(4), 368–377. https://doi.org/10.1002/ppp.1857

Krautblatter, M. (2009). *Detection and quantification of permafrost change in alpine rock walls and implications for rock instability*. Universität Bonn.

Krautblatter, M., & Dikau, R. (2007). Toward a uniform concept for the comparison and extrapolation of rockwall retreat and rockfall supply. *Geografiska Annaler - Series A: Physical Geography*, *89*(1), 21–40. https://doi.org/10.1111/j.1468-0459.2007.00305.x

Krautblatter, M., & Draebing, D. (2014). Pseudo 3-DPwave refraction seismic monitoring of permafrost in steep unstable bedrock. *Journal of Geophysical Research: Earth Surface*, *119*(2), 287–299. https://doi.org/10.1002/2012jf002638

Krautblatter, M., & Moore, J. R. (2014). Rock slope instability and erosion: Toward improved process understanding. *Earth Surface Processes and Landforms*, *39*(9), 1273–1278. https://doi.org/10.1002/esp.3578

Leith, K., Moore, J. R., Amann, F., & Loew, S. (2014). In situ stress control on microcrack generation and macroscopic extensional fracture in exhuming bedrock. *Journal of Geophysical Research: Solid Earth*, *119*(1), 594–615. https://doi.org/10.1002/2012jb009801

Leith, K., Moore, J. R., Amann, F., & Loew, S. (2014). Subglacial extensional fracture development and implications for Alpine Valley evolution. *Journal of Geophysical Research: Earth Surface*, *119*(1), 62–81. https://doi.org/10.1002/2012jf002691

Lepique, M. (2008). Empfehlung Nr. 10 des Arbeitskreises 3.3 "Versuchstechnik Fels" der Deutschen Gesellschaft für Geotechnik e. V.: Indirekter Zugversuch an Gesteinsproben - Spaltzugversuch. *Bautechnik*, *85*(9), 623–627. https://doi.org/10.1002/bate.200810048

Luetschg, M., Lehning, M., & Haeberli, W. (2008). A sensitivity study of factors influencing warm/thin permafrost in the Swiss Alps. *Journal of Glaciology*, *54*(187), 696–704. https://doi.org/10.3189/002214308786570881

Magnin, F., Deline, P., Ravanel, L., Noetzli, J., & Pogliotti, P. (2015). Thermal characteristics of permafrost in the steep alpine rock walls of the Aiguille du Midi. *The Cryosphere*, *9*, 109–121). https://doi.org/10.5194/tc-9-109-2015

Maji, V., & Murton, J. B. (2020). Micro-computed tomography imaging and probabilistic modeling of rock fracture by freeze-thaw. *Earth Surface Processes and Landforms*, *45*(3), 666–680. https://doi.org/10.1002/esp.4764

Marshall, J. A., Roering, J. J., Bartlein, P. J., Gavin, D. G., Granger, D. E., Rempel, A. W., et al. (2015). Frost for the trees: Did climate increase erosion in unglaciated landscapes during the late Pleistocene? *Science Advances*, *1*(10), e1500715. https://doi.org/10.1126/sciadv.1500715

Marshall, J. A., Roering, J. J., Gavin, D. G., & Granger, D. E. (2017). Late Quaternary climatic controls on erosion rates and geomorphic processes in western Oregon, USA. *Geological Society of America Bulletin*, *129*(5–6), 715–731. https://doi.org/10.1130/B31509.1

Marshall, J. A., Roering, J. J., Rempel, A. W., Shafer, S. L., & Bartlein, P. J. (2021). Extensive frost weathering across unglaciated North America during the Last Glacial Maximum. *Geophysical Research Letters*, *48*, e2020GL090305. https://doi.org/10.1029/2020GL090305

Matsuoka, N. (2001). Direct observation of frost wedging in alpine bedrock. *Earth Surface Processes and Landforms*, *26*(6), 601–614. https://doi.org/10.1002/esp.208

Matsuoka, N. (2008). Frost weathering and rockwall erosion in the southeastern Swiss Alps: Long-term (1994-2006) observations. *Geomorphology*, *99*(1–4), 353–368. https://doi.org/10.1016/j.geomorph.2007.11.013

Matsuoka, N. (2019). A multi-method monitoring of timing, magnitude and origin of rockfall activity in the Japanese Alps. *Geomorphology*, *336*, 65–76. https://doi.org/10.1016/j.geomorph.2019.03.023

Matsuoka, N., & Murton, J. (2008). Frost weathering: Recent advances and future directions. *Permafrost and Periglacial Processes*, *19*(2), 195–210. https://doi.org/10.1002/ppp.620

Matsuoka, N., & Sakai, H. (1999). Rockfall activity from an alpine cliff during thawing periods. *Geomorphology*, *28*, 309–328. https://doi.org/10.1016/S0169-555X(98)00116-0

Matthews, J. A., Dawson, A. G., & Shakesby, R. A. (1986). Lake shoreline development, frost weathering and rock platform erosion in an alpine periglacial environment, Jotunheimen, southern Norway. *Boreas*, *15*(1), 33–50. https://doi.org/10.1111/j.1502-3885.1986.tb00741.x

McCarroll, D. (1991). The Schmidt hammer, weathering and rock surface roughness. *Earth Surface Processes and Landforms*, *16*(5), 477–480. https://doi.org/10.1002/esp.3290160510

McGreevy, J. P., & Whalley, W. B. (1985). Rock moisture content and frost weathering under natural and experimental conditions: A comparative discussion. *Arctic and Alpine Research*, *17*(3), 337–346. https://doi.org/10.2307/1551022

Mellor, M. (1970). *Phase Composition of Pore water in Cold rocks*. Hanover: CRREL Research Reports

Messenzehl, K., Viles, H., Otto, J.-C., Ewald, A., & Dikau, R. (2018). Linking rock weathering, rockwall instability and rockfall supply on talus slopes in glaciated hanging valleys (Swiss Alps). *Permafrost and Periglacial Processes*, *29*(3), 135–151. https://doi.org/10.1002/ppp.1976

MeteoSwiss. (2019a). *Climate data station Grächen, 2016-2019. Provided by MeteoSwiss*. Swiss Federal Office of Meteorology and Climatology.

MeteoSwiss. (2019b). *Climate data station Oberer Stelligletscher 2016-2019. Provided by MeteoSwiss*. Swiss Federal Office of Meteorology and Climatology.

Molnar, P., Anderson, R. S., & Anderson, S. P. (2007). Tectonics, fracturing of rock, and erosion. *Journal of Geophysical Research*, *112*(F3). https://doi.org/10.1029/2005JF000433

Montgomery, D. R., & Brandon, M. T. (2002). Topographic controls on erosion rates in tectonically active mountain ranges. *Earth and Planetary Science Letters*, *201*(3), 481–489. https://doi.org/10.1016/S0012-821X(02)00725-2

Moore, J. R., Gischig, V., Katterbach, M., & Loew, S. (2011). Air circulation in deep fractures and the temperature field of an alpine rock slope. *Earth Surface Processes and Landforms*, *36*(15), 1985–1996. https://doi.org/10.1002/esp.2217

Murphy, B. P., Johnson, J. P. L., Gasparini, N. M., & Sklar, L. S. (2016). Chemical weathering as a mechanism for the climatic control of bedrock river incision. *Nature*, *532*(7598), 223–227. https://doi.org/10.1038/nature17449

Murton, J. B., Peterson, R., & Ozouf, J.-C. (2006). Bedrock fracture by ice segregation in cold regions. *Science*, *314*(5802), 1127–1129. https://doi.org/10.1126/science.1132127

Mutschler, T. (2004). Neufassung der Empfehlung Nr. 1 des Arbeitskreises ?Versuchstechnik Fels? der Deutschen Gesellschaft fur Geotechnik e. V.: Einaxiale Druckversuche an zylindrischen Gesteinsprufkorpern. *Bautechnik*, *81*(10), 825–834. https://doi.org/10.1002/bate.200490194

Noetzli, J., & Gruber, S. (2009). Transient thermal effects in Alpine permafrost. *The Cryosphere*, *3*(1), 85–99. https://doi.org/10.5194/tc-3-85-2009

Noetzli, J., Gruber, S., Kohl, T., Salzmann, N., & Haeberli, W. (2007). Three-dimensional distribution and evolution of permafrost temperatures in idealized high-mountain topography. *Journal of Geophysical Research*, *112*, F02S13. https://doi.org/10.1029/2006JF000545

Orr, E. N., Owen, L. A., Saha, S., & Caffee, M. W. (2019). Rates of rockwall slope erosion in the upper Bhagirathi catchment, Garhwal Himalaya. *Earth Surface Processes and Landforms*, *44*(15), 3108–3127. https://doi.org/10.1002/esp.4720

Otto, J.-C., Schrott, L., Jaboyedoff, M., & Dikau, R. (2009). Quantifying sediment storage in a high alpine valley (Turtmanntal, Switzerland). *Earth Surface Processes and Landforms*, *34*(13), 1726–1742. https://doi.org/10.1002/esp.1856

Perras, M. A., & Diederichs, M. S. (2014). A review of the tensile strength of rock: Concepts and testing. *Geotechnical and Geological Engineering*, *32*(2), 525–546. https://doi.org/10.1007/s10706-014-9732-0

Phillips, M., Haberkorn, A., Draebing, D., Krautblatter, M., Rhyner, H., & Kenner, R. (2016). Seasonally intermittent water flow through deep fractures in an Alpine rock ridge: Gemsstock, central Swiss Alps. *Cold Regions Science and Technology*, *125*, 117–127. https://doi.org/10.1016/j.coldregions.2016.02.010

Phillips, M., Haberkorn, A., & Rhyner, H. (2017). Snowpack characteristics on steep frozen rock slopes. *Cold Regions Science and Technology*, *141*, 54–65. https://doi.org/10.1016/j.coldregions.2017.05.010

Priest, S. D. (1993). *Discontinuity analysis for rock engineering*. London, Glasgow: Chapman & Hall. https://doi.org/10.1007/978-94-011-1498-1

Rempel, A. W., Marshall, J. A., & Roering, J. J. (2016). Modeling relative frost weathering rates at geomorphic scales. *Earth and Planetary Science Letters*, *453*, 87–95. https://doi.org/10.1016/j.epsl.2016.08.019

Rengers, F. K., Kean, J. W., Reitman, N. G., Smith, J. B., Coe, J. A., & McGuire, L. A. (2020). The influence of frost weathering on debris flow sediment supply in an Alpine basin. *Journal of Geophysical Research: Earth Surface*, *125*(2), e2019JF005369. https://doi.org/10.1029/2019jf005369

Rode, M., Schnepfleitner, H., & Sass, O. (2016). Simulation of moisture content in alpine rockwalls during freeze-thaw events. *Earth Surface Processes and Landforms*, *41*(13), 1937–1950. https://doi.org/10.1002/esp.3961

Sanders, J. W., Cuffey, K. M., Moore, J. R., MacGregor, K. R., & Kavanaugh, J. L. (2012). Periglacial weathering and headwall erosion in cirque glacier bergschrunds. *Geology*, *40*(9), 779–782. https://doi.org/10.1130/g33330.1

Sass, O. (2005a). Rock moisture measurements: Techniques, results, and implications for weathering. *Earth Surface Processes and Landforms*, *30*(3), 359–374. https://doi.org/10.1002/esp.1214

Sass, O. (2005b). Spatial patterns of rockfall intensity in the northern Alps. *Zeitschrift für Geomorphologie*, *138*, 51–65.

Sass, O. (2005c). Temporal variability of rockfall in the Bavarian Alps, Germany. *Arctic, Antarctic, and Alpine Research*, *37*(4), 564–573. https://doi.org/10.1657/1523-0430(2005)03710.1657/1523-0430(2005)037[0564:tvorit]2.0.co;2

Sass, O. (2007). Bedrock detection and talus thickness assessment in the European Alps using geophysical methods. *Journal of Applied Geophysics*, *62*(3), 254–269. https://doi.org/10.1016/j.jappgeo.2006.12.003

Sass, O. (2010). Spatial and temporal patterns of talus activity - A lichenometric approach in the stubaier alps, austria. *Geografiska Annaler - Series A: Physical Geography*, *92*(3), 375–391. https://doi.org/10.1111/j.1468-0459.2010.00402.x

Savi, S., Delunel, R., & Schlunegger, F. (2015). Efficiency of frost-cracking processes through space and time: An example from the eastern Italian Alps. *Geomorphology*, *232*, 248–260. https://doi.org/10.1016/j.geomorph.2015.01.009

Scandroglio, R., Draebing, D., Offer, M., & Krautblatter, M. (2021). 4D quantification of alpine permafrost degradation in steep rock walls using a laboratory-calibrated electrical resistivity tomography approach. *Near Surface Geophysics*, *19*, 241–260. https://doi.org/10.1002/nsg.12149

Scherler, D. (2014). Climatic limits to headwall retreat in the Khumbu Himalaya, eastern Nepal. *Geology*, *42*(11), 1019–1022. https://doi.org/10.1130/g35975.1

Scherler, D., Bookhagen, B., & Strecker, M. R. (2011). Hillslope-glacier coupling: The interplay of topography and glacial dynamics in High Asia. *Journal of Geophysical Research*, *116*(F2). https://doi.org/10.1029/2010JF001751

Schmid, M.-O., Gubler, S., Fiddes, J., & Gruber, S. (2012). Inferring snowpack ripening and melt-out from distributed measurements of near-surface ground temperatures. *The Cryosphere*, *6*(5), 1127–1139. https://doi.org/10.5194/tc-6-1127-2012

Schrott, L., Hufschmidt, G., Hankammer, M., Hoffmann, T., & Dikau, R. (2003). Spatial distribution of sediment storage types and quantification of valley fill deposits in an alpine basin, Reintal, Bavarian Alps, Germany. *Geomorphology*, *55*(1–4), 45–63. https://doi.org/10.1016/S0169-555X(03)00131-4

Segall, P. (1984). Rate-dependent extensional deformation resulting from crack growth in rock. *Journal of Geophysical Research*, *89*(B6), 4185–4195. https://doi.org/10.1029/JB089iB06p04185

Selby, M. J. (1980). A rock mass strength classification for geomorphic purposes: With tests from Antarctica and New Zealand. *Zeitschrift Fur Geomorphologie*, *24*(1), 31–51.

Shobe, C. M., Hancock, G. S., Eppes, M. C., & Small, E. E. (2017). Field evidence for the influence of weathering on rock erodibility and channel form in bedrock rivers. *Earth Surface Processes and Landforms*, *42*(13), 1997–2012. https://doi.org/10.1002/esp.4163

Statham, I. (1976). A scree slope rockfall model. *Earth Surface Processes*, *1*(1), 43–62. https://doi.org/10.1002/esp.3290010106

Strunden, J., Ehlers, T. A., Brehm, D., & Nettesheim, M. (2015). Spatial and temporal variations in rockfall determined from TLS measurements in a deglaciated valley, Switzerland. *Journal of Geophysical Research: Earth Surface*, *120*(7), 1251–1273. https://doi.org/10.1002/2014jf003274

Thapa, P., Martin, Y. E., & Johnson, E. A. (2017). Quantification of controls on regional rockfall activity and talus deposition, Kananaskis, Canadian Rockies. *Geomorphology*, *299*, 107–123. https://doi.org/10.1016/j.geomorph.2017.09.039

Viles, H. A. (2013). Linking weathering and rock slope instability: Non-linear perspectives. *Earth Surface Processes and Landforms*, *38*(1), 62–70. https://doi.org/10.1002/esp.3294

Walder, J. S., & Hallet, B. (1985). A theoretical model of the fracture of rock during freezing. *The Geological Society of America Bulletin*, *96*(3), 336–346. https://doi.org/10.1130/0016-7606(1985)9610.1130/0016-7606(1985)96<336:atmotf>2.0.co;2

Walder, J. S., & Hallet, B. (1986). The physical basis of frost weathering: Toward a more fundamental and unified perspective. *Arctic and Alpine Research*, *18*(1), 27–32. https://doi.org/10.2307/1551211

Weber, S., Fäh, D., Beutel, J., Faillettaz, J., Gruber, S., & Vieli, A. (2018). Ambient seismic vibrations in steep bedrock permafrost used to infer variations of ice-fill in fractures. *Earth and Planetary Science Letters*, *501*, 119–127. https://doi.org/10.1016/j.epsl.2018.08.042

Wegmann, M. (1998). *Frostdynamik in hochalpinen felswänden am Beispiel der region Jungfraujoch - aletsch. (PhD thesis)*. Zürich.

Wegmann, M., & Gudmundsson, G. H. (1999). *Thermally induced temporal strain variations in rock walls observed at subzero temperatures*. In K. Hutter, Y. Wang, & H. Beer (Eds.), Advances in Cold-Region thermal Engineering and Sciences (Vol. 533, pp. 511–518). Berlin, Heidelberg: Springer. https://doi.org/10.1007/BFb0104208

Wegmann, M., Gudmundsson, G. H., & Haeberli, W. (1998). Permafrost changes in rock walls and the retreat of alpine glaciers: A thermal modeling approach. *Permafrost and Periglacial Processes*, *9*, 23–33. https://doi.org/10.1002/(SICI)1099-1530(199801/03)10.1002/(sici)1099-1530(199801/03)9:1<23::aid-ppp274>3.0.co;2-y

Wegmann, M., & Keusen, H.-R. (1998). Recent geophysical investigations at a high alpine permafrost construction site in Switzerland. Paper presented at the 7th International Conference on Permafrost Yellowknife. Canada.

Whipple, K. X., Kirby, E., & Brocklehurst, S. H. (1999). Geomorphic limits to climate-induced increases in topographic relief. *Nature*, *401*(6748), 39–43. https://doi.org/10.1038/43375

Wirz, V., Schirmer, M., Gruber, S., & Lehning, M. (2011). Spatio-temporal measurements and analysis of snow depth in a rock face. *The Cryosphere*, *5*(4), 893–905. https://doi.org/10.5194/tc-5-893-2011

Zhang, Z. X. (2002). An empirical relation between mode I fracture toughness and the tensile strength of rock. *International Journal of Rock Mechanics and Mining Sciences*, *39*(3), 401–406. https://doi.org/10.1016/S1365-1609(02)00032-1